POLITECNICO DI MILANO
Master of Science in Computer Engineering
Scuola di ingegneria dell'Informazione

POLO TERRITORIALE DI COMO

Modal analysis of arbitrary surfaces through dictionary-based near-field acoustic holography

Thesis Supervisor: Prof. Fabio Antonacci
Assistant Supervisor: Dr. Antonio Canclini

Candidate: Massimo Varini
Student Id. number: 797309

Academic Year 2015-2016

POLITECNICO DI MILANO
Corso di Laurea Magistrale in Ingegneria Informatica
Scuola di ingegneria dell'Informazione

POLO TERRITORIALE DI COMO

Analisi modale di superfici arbitrarie mediante olografia acustica, in campo vicino, basata su dizionario

Relatore: Prof. Fabio Antonacci
Correlatore: Dr. Antonio Canclini

Candidato: Massimo Varini
Matricola: 797309

Anno Accademico 2015-2016

To my family and Daniela

Sommario

In questa tesi proponiamo una nuova metodologia per effettuare analisi modale partendo da misure acustiche mediante olografia acustica in campo vicino. Per fare questo, la nostra tecnica combina il metodo delle sorgenti equivalenti (ESM) con i vantaggi dati dal cercare la soluzione in un dominio sparso sfruttando una conoscenza pregressa. In particolare, viene cercata una soluzione sparsa in uno spazio identificato da un dizionario pre-calcolato. Le componenti del dizionario sono i pesi delle sorgenti equivalenti. Pertanto, la soluzione al problema è ottenuta individuando la miglior combinazione lineare possibile di pesi delle sorgenti equivalenti presenti nel dizionario, in accordo alle misure acustiche effettute.

Un approccio basato su dizionario permette di ridurre significativamente il numero di microfoni necessari, pertanto è possibile ridurre i costi del sistema di acquisizione audio, ridurre la complessità del cablaggio e ridurre i problemi relativi al supporto sul quale ancorare i microfoni. Inoltre, questo tipo di approccio, intrinsecamente rende la tecnica proposta robusta rispetto al rumore di misura. La nostra tecnica non richiede quindi che le misure vengano effettuate in una camera anecoica.

Per la validazione del nostro metodo usiamo misure di pressione acustica, acquisite in campo vicino, relative ad un pannello vibrante rettangolare di alluminio. Le misure sono state acquisite in un ambiente non ideale (i.e., non anecoico), pertanto un certo livello di riverberazione e rumore di fondo sono presenti. I risultati sperimentali confermano che la nostra tecnica riesce a ricostruire i modi di vibrazione del pannello usando un numero limitato di microfoni. Inoltre la metodologia proposta mostra un comportamento robusto in presenza di rumore di misura.

Infine presentiamo i risultati ottenuti da simulazioni effettuate su una tavola di violinio vibrante, per testare l'idoneità del nostro metodo per l'analisi di superfici complesse. I risulati sono promettenti, infatti dimostrano che il nostro metodo dà prestazioni migliori rispetto al metodo ESM, sia usando un numero limitato di microfoni, sia in presenza di rumore di misura.

Abstract

In this thesis we propose a novel methodology to perform modal analysis starting from acoustic measurements using near-field acoustic holography. To do this, our technique combines the Equivalent Source Method (ESM) with the advantages of searching the solution in a sparse domain using some a priori knowledge. In particular, a sparse solution is searched in a space spanned by a pre-computed dictionary. The entries of the dictionary are the equivalent source weights. Therefore, the solution to the problem is obtained searching the better linear combination of the equivalent source weights in the dictionary, according to the acoustic measurements.

Using a dictionary based approach makes possible to significantly reduce the number of required microphones, therefore it is possible to reduce the cost of the microphones acquisition system, to reduce the wiring complexity and the problem related to the microphones standing.

Moreover, the dictionary approach intrinsically makes the technique robust against measurement noise. Thanks to this our techniques does not require that the acoustic measurements have to be acquired into an anechoic chamber.

To validate our method we use real acoustic pressure measurements acquired in the near-field of a vibrating aluminium rectangular plate. The measurements are acquired in a non-ideal room (i.e., non anechoic), therefore some amount of reverberation and background noise are present. Experimental results confirm that our technique can reconstruct the vibration modes of the plate using a limited number of microphones. Moreover the methodology shows a robust behaviour in the presence of measurement noise.

We also present simulative results related to a vibrating violin top plate, to test the suitability of the method for analysing complex surfaces. Results are promising as they show that our method outperforms the classical ESM technique, even using a limited number of microphones and in the presence of measurement noise.

Acknowledgements

I would like to thank my thesis supervisor, Prof. Fabio Antonacci, who offered me an interesting research activity-

A very special thanks goes to Dr. Antonio Canclini, who supported me as well with his precious suggestions and great helpfulness, even during the most difficult times.

A special thanks goes to my parents Mirella and Orlando, and to my sisters Marta, Alessandra and Chiara for their support during my studies.

The deepest and most special thanks goes to Daniela, for always standing by my side and helping keeping me serene, even when problems and worries seemed to be insurmountable.

Finally a special thanks goes to my grandfather who would have wanted to be here.

Contents

List of Figures

List of Tables

Chapter 1

Introduction

Modal analysis aims at studying the dynamic properties of a structure under vibrational excitation. A typical task is that of identifying the resonance frequencies of a vibrating surface, along with the corresponding modes of vibration. Modal analysis finds application in different fields, ranging from automotive, avionic, structural engineering, to mechanics and vibro-acoustics. For instance, by analysing how a car engine vibrates, it is possible to identify the areas that contribute the most to noise production. Similarly, modal analysis of musical instruments can be useful to understand how sound is generated and propagates.

In this thesis we focus on modal analysis of surfaces with arbitrary geometries, and we are particularly interested in techniques that are minimally invasive. Non-invasiveness is a requirement whenever the surface under analysis is delicate (e.g., fragile plates of historical musical instruments, thinly varnished objects, etc.).

Modal analysis can be accomplished by means of several techniques that are characterized by different degrees of invasivity, involving different types of sensors. We can broadly distinguish them into contact and contactless measurement systems. Contact methods are mainly accomplished by means of accelerometric sensors; contactless methods include laser-vibrometric analysis and near-field acoustic holography.

The accelerometric analysis is a contact method analysis that performs direct measurements. It is based on accelerometers which measure the acceleration of the object with which they are put in contact. This technique is moderately expensive and it gives good results in terms of precision and frequency interval analysis. However, since the sensors need to be attached, glued, to the structure undergoing test, is absolutely not usable if we want to analyse delicate objects.

The laser-vibrometer technique is a contactless method that performs direct measurements. This method uses laser-vibrometer and it is based on doppler effect. This analysis system, differently from the previous case, does not need to enter in contact with the object in order to perform measurements, so there are no risks of damaging the structure. Furthermore, not charging the structure from an inertial point of view, the analysis can be performed also on very small objects. The downside is that a laser-vibrometer is very expensive so it is not an instrument easily available; furthermore it can have problems to perform measurements on highly reflective varnished surfaces.

An interesting alternative to the classical vibrometric approaches is near-field acoustic holography (NAH). It constitutes a good tradeoff between the measurement accuracy and the cost of the required hardware. Measurements are performed by means of a microphone array and the data acquired (acoustic pressure), properly processed, can be used to estimate the velocity or displacement of the surface of the structure under test. Since measurements are made by microphone array we have to prevent acoustic noise, therefore they have to be performed in a room where acoustic is controlled (anechoic chamber).

NAH is a well established technique in literature for the analysis of planar surfaces, for which the solution is generally based on the inversion of the first Rayleigh's integral [1]. Conversely, the case of more complex surfaces (i.e., curved, non-convex, etc.) is still an active field of research. In the literature we could find different techniques, but first of all it is necessary to make a distinction between planar and non-planar techniques. Planar techniques have got as fundamental assumption that the source geometry must be planar or locally planar.

The method proposed by Williams and Maynard [1], based on the Rayleigh's Integrals, described in Sec. 2.3, belongs to planar techniques. Another technique that treats planar geometries is the one proposed in [2]. This technique is focused on exploiting some a-priori knowledge to find the optimal solution to the problem. The authors used some well known basis functions, that can be computed analytically, to explain the problem. They used these functions to build a dictionary that allow them to search the solution to the problem in a sparse domain, and not in a general one.

Regarding the techniques extendible to non-planar surfaces, reference may be made to inverse Boundary Element Method (iBEM) [3]. This technique is based on inversion of BEM, which is a numerical method to solve radiation problems, based on partial differential equations with integral formulation. Another technique for non-planar near-field acoustic holography

is that based on the ESM (Equivalent Source Method) [4]. This method is strictly related to iBEM, since originally ESM was developed as an alternative to BEM to provide a numerical (approximated) solution to the radiation problem in an efficient way from the computational point of view. The ESM models the acoustic pressure generated by a vibrating source as the sound field obtained by superposing the effect of a set of equivalent virtual sources located within the source itself. ESM-based NAH operates in two steps. The first step involves the solution of an inverse problem to find the strength (complex weights) of the equivalent sources that generate the measured acoustic pressure. Then, a suitable propagator function is applied to the equivalent sources, in order to infer the velocity on the surface of the vibrating source. The ESM-based NAH seems adequate to our needs because it works for arbitrary geometries and it is efficient from a computational point of view. On the other hand the ESM does not consider a sparse domain.

In this thesis we propose a novel technique for NAH, which combines the flexibility of the ESM with the advantages of seeking the solution in a sparse domain. The proposed technique aims at being robust in those situations where it is not possible to use a great number of sensors (i.e. microphones) and in the presence of measurement noise (e.g., the proposed methodology could work also in a room not necessarily anechoic). In this way, it is possible to keep moderate the hardware costs implied by very large microphone systems and by the building/renting an anechoic chamber. We suggest a solution that takes advantage of some a priori knowledge to solve the problem. Indeed, we observed that, even for complex surfaces, the shape of vibration modes is mainly determined by the geometry of the vibrating surface. Conversely, vibration modes are substantially invariant with respect to the physical parameters of the surface material (e.g. density, Young's modulus, Poisson's ratio, etc.). We also observed that this invariance is maintained also by the corresponding equivalent sources. This fact can therefore be exploited to restrict the solution space of the classical ESM formulation. More specifically, we first numerically predict a set of possible vibration modes through Finite Element Analysis (FEA) varying the physical parameters in a large range. This information is then turned into a set of equivalent sources and associated weights, from which a compressed dictionary is computed by selecting the principal components of the weights. NAH is finally accomplished by finding a sparse linear combination of the dictionary entries.

For the validation of our method we considered real acoustic measurements acquired in the near-field of a vibrating aluminium rectangular plate.

More specifically, we considered a public dataset [2] targeted for NAH experiments. The results of the proposed technique was compared with the ground-truth provided in the dataset. Experimental results show that the proposed technique is capable of reconstructing the plate vibration modes even with a limited number of microphones. The technique also turns out to be robust against measurement noise.

In the perspective of analysing more complex surfaces, we consider an example scenario. We focus on the modal analysis of acoustic musical instruments. This scenario is particularly interesting, as instruments sound quality strongly depends on even subtle geometrical details. As a study case, we tested the proposed technique for analysing the vibration modes of a violin top plate. To this end, we performed a set of numerical simulations to obtain synthetic measurements of the acoustic pressure. These synthetic measurements, along with the geometrical model of the violin plate, were used to accomplish NAH by means of the proposed method. Results are promising, as they show that the dictionary-based ESM approach outperforms the standard ESM method, even in the presence of measurement noise and disposing of a limited number of microphones.

In Chapter 2 we will introduce some fundamental notion about physical acoustics.

In Chapter 3 we will discuss the State of the Art, we will describe in detail the planar NAH techniques and non-planar NAH techniques. In particular we will focus our attention to the classical implementation of the ESM.

Chapter 4 is the core of this thesis, here we will introduce our method. After a general overview we will explain in detail each aspect of our work starting from the FEM analysis, to the construction of the dictionary and finally the modes of vibration.

In Chapter 5 we will provide details about the realization of the system, describing the main tools used for the involved tasks.

In Chapter 6 we validate the proposed method, showing the results for real data. Moreover we present the simulation result for a complex surface as is the violin top plate.

In Chapter 7 we will draw some final conclusions and we will indicate some future outlooks.

Chapter 2

Fundamentals of physical acoustics

In this chapter we introduce some preliminary notions about physical acoustics, in particular we deal with Wave equation and Helmholtz equation, these two equations allow us to describe an acoustic wave. After that we introduce Green Functions and Kirchhoff-Helmholtz Integral Equation (HIE). HIE, with the aid of the Green Functions, describes how a vibrating source radiates in the space relying on surface pressure or normal velocity of the source. In some simple cases, instead, there are analytic solutions (e.g planar geometries) so we introduce the First and Second Rayleigh's integrals and as a particular case we illustrate how a simply supported rectangular plate vibrates.

2.1 Wave equation, Helmholtz equation and Green's function

The wave equation, also known as D'Alembert's equation, describes the propagation of a wave as a function of spatial and temporal coordinates.

Let us first introduce the time-space reference system. We denote with t the time coordinate, while a 3D point is described by the vector $\mathbf{x} = [x, y, z]^T$ in Cartesian coordinates or by $\mathbf{r} = [\rho, \theta, \varphi]^T$ in spherical coordinates. The distance of the point, identified by the position vector $\mathbf{r}$, from the origin is ρ; φ is the angle between the x-axis and the projection of the vector $\mathbf{r}$ on the xy plane and θ is the angle between the z-axis anche vector $\mathbf{r}$. The Cartesian and polar coordinates are related by

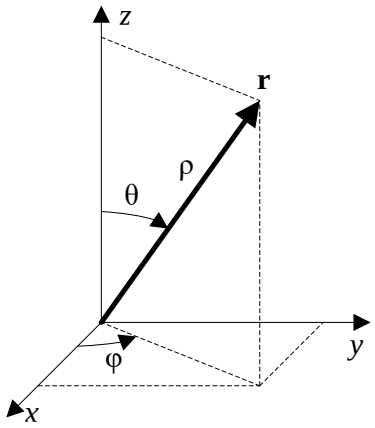

Figure 2.1: Cartesian and spherical coordinates system

$$\mathbf{x} = \rho \begin{bmatrix} \sin\theta\cos\varphi \\ \sin\theta\sin\varphi \\ \cos\theta \end{bmatrix} \qquad \text{and} \qquad \mathbf{r} = \begin{bmatrix} \sqrt{x^2+y^2+z^2} \\ \arctan\left(y/x\right) \\ \arccos\left(z/\sqrt{x^2+y^2+z^2}\right) \end{bmatrix}. \quad (2.1)$$

The wave equation, in its homogeneous form, is a partial differential equation of the function $p(\mathbf{x}, t)$ or equivalently $p(\mathbf{r}, t)$ that depends from spatial and temporal coordinates as follows

$$\nabla^2 p(\mathbf{r}, t) - \frac{1}{c^2}\frac{\partial^2}{\partial t^2} p(\mathbf{r}, t) = 0, \qquad \mathbf{r} \in V, \quad (2.2)$$

whose solutions are called sound fields. The function $p(\mathbf{r}, t)$, in this case, represents the acoustic pressure and describes its spatial distribution in all the points identified by the position vector $\mathbf{r}$. The domain of the wave equation is restricted to a volume V in which no sources are present. The term c is the propagation speed, and $c \approx 343 m/s$ for sound in air at 20 °C.

A simple solution to Eq. (2.2) is given by plane waves which propagate with velocity c in the direction identified by the normal vector $\mathbf{n}$,

$$p(\mathbf{r}, t) = g\left(t + \frac{1}{c}\mathbf{n}^T\mathbf{r}\right) \quad (2.3)$$

where the superscript ^{T} indicates the vector transposition. The argument of the function g is a plane in space with normal vector $\mathbf{n}$, for this reason we refer to $p(\mathbf{r}, t)$ as plane waves. Increasing time t, the plane waves propagate through space with speed c. If we apply the Fourier transform to Eq. (2.3) we obtain the sound pressure distribution in the frequency domain. Doing the same operation with Eq. (2.2) we derive the Homogeneous Helmholtz equation,

$$\nabla^2 P(\mathbf{r}, \omega) + k^2 P(\mathbf{r}, \omega) = 0, \quad (2.4)$$

where $k = \omega/c = 2\pi f/c$ is the wave number and f is the frequency. One possible solution to the homogeneous Helmholtz equation has the form

$$P(\mathbf{r}, \omega) = A(\omega)e^{j\mathbf{kr}}, \tag{2.5}$$

where $A(\omega)$ is an arbitrary constant and $\mathbf{k}$ is the wave vector defined as

$$\mathbf{k} = \begin{bmatrix} k\sin\theta\cos\varphi \\ k\sin\theta\sin\varphi \\ k\cos\theta \end{bmatrix} \tag{2.6}$$

and it is related to the wave number by the *dispersion relation*

$$k^2 = k_x^2 + k_y^2 + k_y^2. \tag{2.7}$$

where k_x, k_y and k_z are the components of the wave vector $\mathbf{k}$.

The solution $P(\mathbf{r}, \omega)$, in Eq. (2.5), can be seen as a plane waves solution of Eq. (2.4). Rewriting the constant $A(\omega)$ as

$$A(\omega) = 2\pi B(\omega)\delta(\omega - \omega_0), \tag{2.8}$$

replacing it in Eq. (2.5) and taking the inverse Fourier transform yields to the final result

$$p(\mathbf{r}, t) = 2\pi B(\omega_0)e^{j(\mathbf{kr}-\omega_0 t)}, \tag{2.9}$$

a plane wave at frequency ω_0, where $k = \omega_0/c$ and $B(\omega_0)$ is a constant.

The wave front is a surface over which a wave has a constant phase. In this case the wave front is planar since the phase term $(\mathbf{kr} - \omega_0 t)$ is constant on planes, Fig. 2.1(a), which are parallel to the one in the origin determined by the product $\mathbf{kr}$. The direction of the wave is defined by the wave vector $\mathbf{k}$ and the wave length is given by $\lambda = c/f$.

It is important to underline the fact that the waves propagate only if $k_x^2 > 0$, $k_y^2 > 0$ and $k_z^2 > 0$. The dispersion relation, Eq. (2.7), is still valid also if one of the terms k_x, k_y or k_z is imaginary (i.e., $k_x^2 < 0$, $k_y^2 < 0$ or $k_z^2 < 0$). In this case the wave does not propagate and it is called evanescent. Evanescent waves are waves that have an amplitude exponential decay moving away from the source, as depicted in Fig. 2.1(b), and have the form

$$p(\mathbf{r}, t) = Ae^{-k'_z z}e^{k_x x + k_y y}, \tag{2.10}$$

where k'_z is defined as

$$k_z = \pm j\sqrt{k_x^2 + k_y^2 - k^2} = \pm jk'_z. \tag{2.11}$$

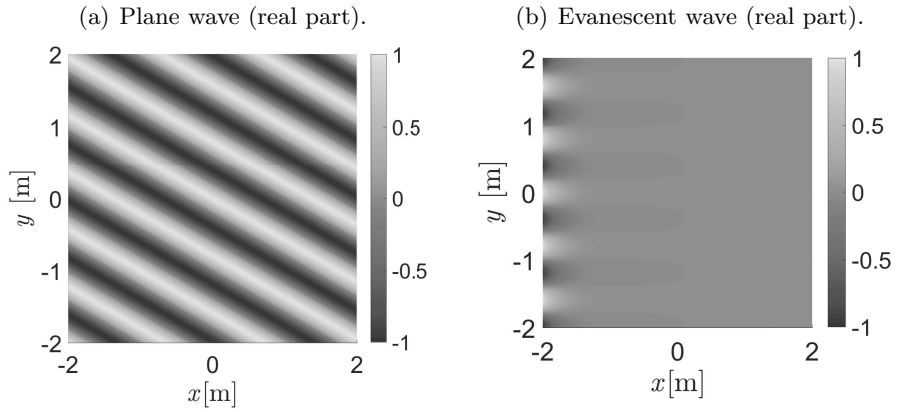

Figure 2.2: Acoustic field of a propagating plane wave and of an evanescent wave. The wave vectors are $\mathbf{k} = k[1/2, \sqrt{3}/2, 0]^T$ *and* $\mathbf{k} = k[j1/2, \sqrt{3}/2, 0]^T$ *respectively,* $k = \omega_0/c$, $\omega_0 = 2\pi f$, $f = 500\,Hz$, $c = 343\,m/s$.

Evanescent waves are also called inhomogeneous waves and they are very important in radiation problems and also in NAH problems. In NAH problems, we must position the microphone array in near-field to measure these waves. If we do not acquire them we cannot reconstruct correctly the source velocity.

Now we consider the case when there are one or more point source $P_0(\mathbf{r}, \omega)$ in the domain V. The Eq. (2.4) is modified as

$$\nabla^2 P(\mathbf{r}, \omega) + k^2 P(\mathbf{r}, \omega) = P_0(\mathbf{r}, \omega). \tag{2.12}$$

In an analogous way Eq. (2.2) will have a not null right-hand member. Solutions to Eq. (2.12) are defined starting from a basic solution obtained by imposing a spatial impulse located at $\mathbf{r}'$ as excitation term,

$$P_0(\mathbf{r}, \omega) = \delta(\mathbf{r} - \mathbf{r}')\delta(\omega) \tag{2.13}$$

where $\delta(\cdot)$ is the Dirac delta function. The solution to Eq. (2.12) is the sound field $G(\mathbf{r}|\mathbf{r}', \omega)$ measured in the point $\mathbf{r}$ due to the spatial impulse located at $\mathbf{r}'$ obtained upon substituting Eq. (2.13) into Eq. (2.12)

$$\nabla^2 G(\mathbf{r}|\mathbf{r}', \omega) + k^2 G(\mathbf{r}|\mathbf{r}', \omega) = \delta(\mathbf{r} - \mathbf{r}'). \tag{2.14}$$

For free field sound propagation the function is given as [1]

$$G(\mathbf{r}|\mathbf{r}', \omega) = \frac{1}{4\pi} \frac{e^{-jk|\mathbf{r}-\mathbf{r}'|}}{|\mathbf{r} - \mathbf{r}'|}. \tag{2.15}$$

and it is called Green's function. Green's functions are also called propagators since allow us to propagate the acoustic field of a point source located at $\mathbf{r}'$ in a point $\mathbf{r}$ of the space.

2.2 Huygens's principle and Kirchhoff-Helmholtz integral

The acoustic source $P_0(\mathbf{r}, \omega)$, introduced in the previous section, could not be a point source and therefore could have an arbitrary geometry. When an object vibrates the air particles around it are compressed or rarefied, thus creating areas in which there is an increase or a decrease of pressure. Because of this it creates a "domino" effect with other air particles and thus the initial vibration induced by the object propagates in the air. In an analogous way the air particles vibrating in an acoustic field produce a force, as pressure variation, on the surface of the object that starts to vibrate.

The solution of Eq. (2.14) allows to compute the sound field generated from a distribution of one or more sources in the volume V. However, it exists an indirect method to compute the sound field by means of the Huygens's principle. The Huygens's principle states that *the new wave front at a later time is the envelope of the fronts of these secondary waves.*

Starting from the Green's theorem we can derive the Kirchhoff-Helmholtz integral that could be considered as a superposition of contributions emitted by a sources on a virtual surface [5].

2.2.1 Green's theorem

Let V be a three-dimensional volume bounded by the surface ∂V and as usual, $\mathbf{r}$ is a vector that identifies a point inside the volume. Let $\Psi(\mathbf{r})$ and $\Upsilon(\mathbf{r})$ be two unknown functions which are finite and continuous with their first and second partial derivatives inside V. We can write Green's theorem (Green's second identity) [1] as

$$\iiint_V \left(\Upsilon \nabla^2 \Psi - \Psi \nabla^2 \Upsilon\right) dV = \iint_{\partial V} \left(\Upsilon \frac{\partial \Psi}{\partial n} - \Psi \frac{\partial \Upsilon}{\partial n}\right) d\partial V, \tag{2.16}$$

where $\frac{\partial}{\partial n}$ is the derivative with respect to the outward normal $\mathbf{n}$. If we assume that the two functions $\Psi(\mathbf{r})$ and $\Upsilon(\mathbf{r})$ also satisfy the homogeneous Helmholtz equation, Eq. (2.4), on the surface ∂V and in the volume V, after some passages we can write

$$\iint_{\partial V} \left(\Upsilon \frac{\partial \Psi}{\partial n} - \Psi \frac{\partial \Upsilon}{\partial n}\right) d\partial V = 0. \tag{2.17}$$

This equation forms the basis for the Kirchhoff-Helmholtz integral equation.

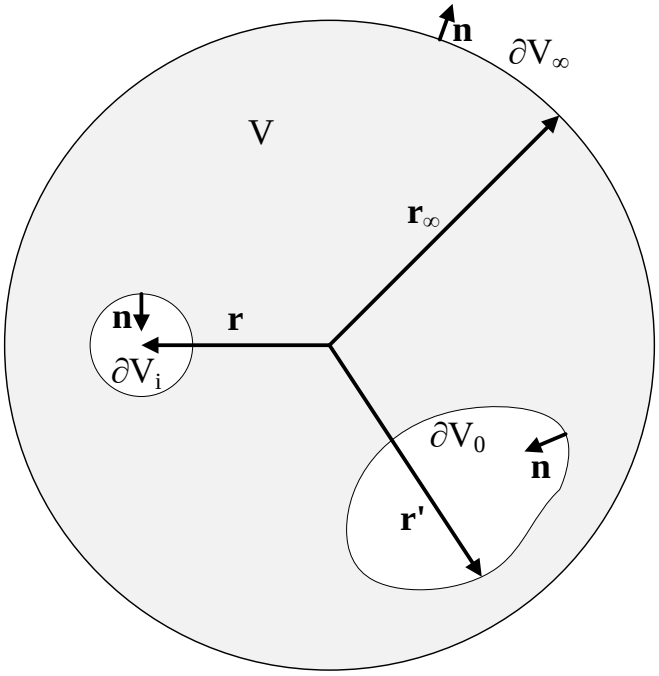

Figure 2.3: Region for the application of the Green's theorem.

2.2.2 Kirchhoff-Helmholtz integral equation

To derive the Kirchhoff-Helmholtz integral equation we define the following region for the application of the Green's theorem, Eq. (2.16). With reference to Fig. 2.3, ∂V_0 is the surface of the object of interest, with arbitrary geometry, where the points on its surface are identified by the position vector $\mathbf{r}'$. The vanishingly spherical surface ∂V_i is the surface that surrounds the evaluation point $\mathbf{r}$ and ∂V_∞ is the outer surface of radius $\mathbf{r}_\infty$ which tends to infinity. The total surface which has to be considered for the application of the Green's theorem is therefore

$$\partial V = \partial V_0 + \partial V_i + \partial V_\infty. \tag{2.18}$$

Starting from Eq. (2.17) and choosing $\Psi = G(\mathbf{r}|\mathbf{r}', \omega)$ the free space Green function defined in Eq. (2.15) and $\Upsilon = P(\mathbf{r}', \omega)$ the pressure distribution on the surface ∂V_0, it can be demonstrated [1] that

$$P(\mathbf{r}, \omega) = \oint_{\partial V} \left(\frac{\partial}{\partial \mathbf{n}} G(\mathbf{r}|\mathbf{r}', \omega) P(\mathbf{r}', \omega) - G(\mathbf{r}|\mathbf{r}', \omega) \frac{\partial}{\partial \mathbf{n}} P(\mathbf{r}', \omega) \right) d\mathbf{r}'. \tag{2.19}$$

This last equation is the Kirchhoff-Helmholtz integral. The Kirchhoff-Helmholtz integral has a fundamental role in extending the NAH to geome-

tries with arbitrary shape since it relates pressure and pressure gradient on the object surface with the pressure in a point in the volume V.

We recall the Euler's equation

$$\rho_0 \frac{\partial \mathbf{v_n}}{\partial t} = -\frac{\partial}{\partial \mathbf{n}} P, \tag{2.20}$$

where $\rho_0 \approx 1.2\ \mathrm{kg/m^3}$ is the air density at 20 ℃ and v_n is the normal velocity of the source. The Euler's equation, Eq. (2.20), relates the pressure gradient with the normal velocity. Moreover the Kirchhoff-Helmholtz integral is the basis of the equivalent source method [4], described later in Chapter 3.

2.3 Rayleigh's integrals

When the vibrating object has a planar geometry, we can use simple equations to compute the pressure distribution in the evaluation point generated from the source.

Rayleigh's integrals are two functions that allow us to relate pressure or normal velocity on a plane to pressure in an another plane. The pressure field can be expressed as

$$p(x, y, z) = \frac{1}{4\pi^2} \int_{-\infty}^{\infty} \int_{-\infty}^{\infty} P(k_x, k_y) e^{j(\mathbf{kr})}\, dk_x\, dk_y. \tag{2.21}$$

We recall that $k_z = \pm\sqrt{k^2 - k_x^2 - k_y^2}$. If we consider only the positive solution it means that the sources are in the half-space $z \leq 0$ so plane waves cannot travel in negative z direction. Now, posing $z = 0$, Eq. (2.21) becomes

$$p(x, y, 0) = \frac{1}{4\pi^2} \int_{-\infty}^{\infty} \int_{-\infty}^{\infty} P(k_x, k_y) e^{j(k_x x + k_y y)}\, dk_x\, dk_y \tag{2.22}$$

where we have made explicit the position and wave vectors, $\mathbf{r}$ and $\mathbf{k}$, and the dot product $\mathbf{kr}$ between them. Eq. (2.22) expresses the pressure distribution in an infinite plane at $z = 0$. Looking at Eq. (2.22) we can recognize that the integrals are two inverse Fourier transforms. If we consider the corresponding two-dimensional Fourier transform we can define the complex amplitude

$$P(k_x, k_y) = \int_{-\infty}^{\infty} \int_{-\infty}^{\infty} p(x, y, 0) e^{-j(k_x x + k_y y)}\, dx\, dy. \tag{2.23}$$

$P(k_x, k_y)$ is called *angular spectrum*. Once $P(k_x, k_y)$ is known, computed by the pressure distribution in the plane $z = 0$, we can compute the pressure field, by means of Eq. (2.21), over the three-dimensional volume from $z = 0$

to infinity. In an analogous way, we can express the angular spectrum in a plane, starting from the angular spectrum in the plane $z = z'$ by

$$P(k_x, k_y, z) = P(k_x, k_y, z')e^{jk_z(z-z')}. \tag{2.24}$$

Now starting from the inverse Fourier transform of this last equation and using some of its properties we can derive the two Rayleigh's integrals [1]

$$p(x, y, z) = -\frac{j\rho_0 ck}{2\pi} \int_{-\infty}^{\infty} \int_{-\infty}^{\infty} v_n(x', y', z') \frac{e^{jk|\mathbf{r}-\mathbf{r}'|}}{|\mathbf{r}-\mathbf{r}'|} \, dx'dy' \tag{2.25}$$

and

$$p(x, y, z) = -\frac{1}{2\pi} \int_{-\infty}^{\infty} \int_{-\infty}^{\infty} p(x', y', z') \frac{\partial}{\partial z'} \left(\frac{e^{jk|\mathbf{r}-\mathbf{r}'|}}{|\mathbf{r}-\mathbf{r}'|} \right) dx'dy'. \tag{2.26}$$

Knowing the normal velocity of the source, by means of Rayleigh's first integral, Eq. (2.25), it is possible to compute the pressure distribution in each point of the space. It is precisely the inversion of this integral that lays the foundations for the NAH [1], described later in Chapter 3. NAH aims at reconstructing the source normal velocity starting from the pressure measured on a plane above it.

2.3.1 Simply supported plate

If we are dealing with simple geometries [6], Rayleigh's integrals can be computed analytically. An interesting case is that of a rectangular plate.

Let us now consider a rectangular plate with dimension L_x and L_y. The equation which describes its motion is

$$\nabla^4 \xi(x, y, \omega) - k_f^4 \xi(x, y, \omega) = 0; \tag{2.27}$$

where $\xi(x, y)$ represents the displacement, $\nabla^4 = \left(\frac{\partial^2}{\partial x^2} + \frac{\partial^2}{\partial y^2} \right)^2$ and the bending wave number is k_f. Let the plate be *simply supported* so the boundary conditions are

$$\begin{aligned} \xi(x, y) = M_x(x, y) = 0 \qquad &\text{for} \qquad x = 0 \text{ and } L_x, \\ \xi(x, y) = M_y(x, y) = 0 \qquad &\text{for} \qquad y = 0 \text{ and } L_y, \end{aligned} \tag{2.28}$$

M_x and M_y are the bending moments. The solution to Eq. (2.27) leads to the function $\Phi_{mn}(x, y)$ that describes the modes shape,

$$\Phi_{mn}(x, y) = \frac{2}{\sqrt{L_x L_y}} \sin(m\pi x/L_x) \sin(n\pi y/L_y). \tag{2.29}$$

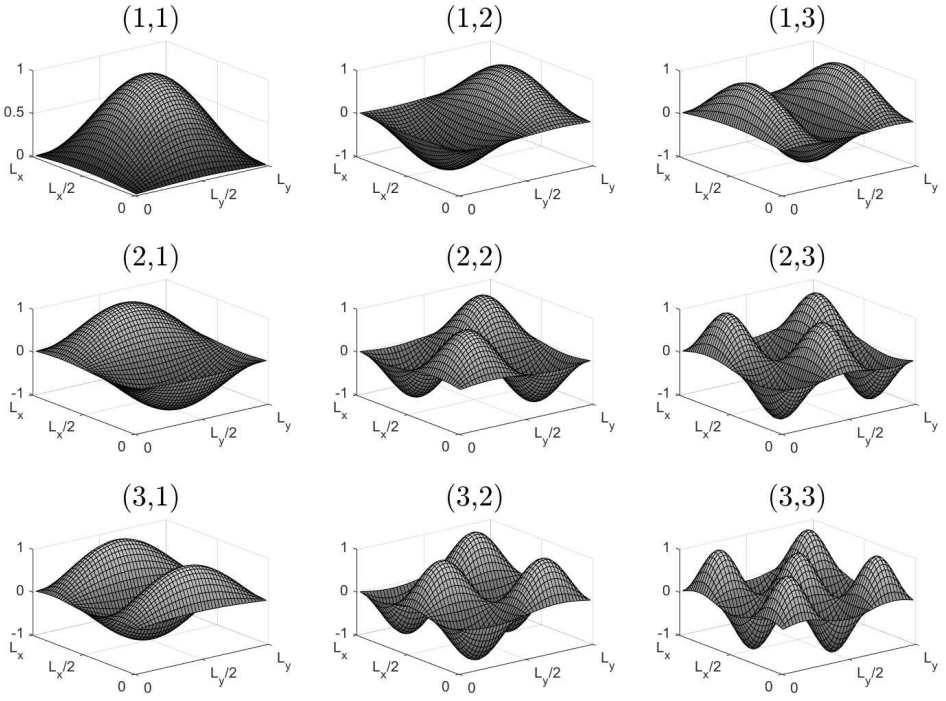

Figure 2.4: Mode shapes for the first nine modes of a simply supported rectangular plate with dimension L_x, L_y and thickness h.

with $m, n \in \mathbb{N}^+$. Some example mode shapes are depicted in Fig. 2.4. The complexity of the mode shapes grows with the modes order (m, n). The function $\Phi_{mn}(x, y)$ satisfies the boundary conditions in Eq. (2.28) and also the equation of motion, Eq. (2.27), only at the eigen frequency

$$\omega_{mn} = \alpha^2[(m\pi/L_x)^2 + (n\pi/L_y)^2]. \tag{2.30}$$

where α is the Skudrzyk's constant [1] defined as

$$\alpha = \left(\frac{D}{\rho_s h}\right)^{1/4} = \left(\frac{Eh^2}{12\rho_s(1-\nu^2)}\right)^{1/4} \tag{2.31}$$

where D is the flexural rigidity, E is the Young's module, ν is the Poisson's ratio, ρ_s is the density of the material and h is the thickness of the plate.

It is important to note that the modes shape depends only on the geometry parameters L_x and L_y of the plate, so is invariant with respect to the variation of the physical parameters of the material. The eigen frequency, instead, depends on the physical parameters of the material because are included in the Skudrzyk's constant.

Now, knowing the functions that describe the modes shape and the relative eigen frequencies we can write the equation that describes the displacement of the plate as a function of the spatial coordinates and of frequency

$$\xi(x, y, \omega) = -\frac{F}{\rho_s h} \sum_{m=1}^{\infty} \sum_{n=1}^{\infty} \frac{\Phi_{mn}(x_0, y_0)\Phi_{mn}(x, y)}{\omega^2 - \omega_{mn}^2}, \tag{2.32}$$

where $F \triangleq |F(\omega)e^{-j\omega t}|$ is the force with which the plate was excited in a point located at (x_0, y_0). Deriving the previous equation we obtain the plate velocity

$$v_n(x, y, \omega) = -j\omega\xi(x, y, \omega). \tag{2.33}$$

Knowing the velocity v_n we can use the first Rayleigh's integral to compute the pressure in the space generated by the rectangular plate. As previously said, the velocity can be computed analytically only for simple geometries, in all other cases we have to use numerical methods, such as FEM, to compute it.

Chapter 3

State of the Art

Near-field acoustic holography is a well known technique for planar geometries. Conversely, the case of more complex surfaces, still remains an active field of research. In this chapter we analyse some techniques for planar geometries and in a second stage we focus our attention on which ones may allow us to extend the field of application to complex surfaces.

3.1 Planar Near-field Acoustic Holography

Before discussing in detail what Acoustic Holography and Near-field Acoustic Holography are, we have to introduce some preliminary notions. With reference to Fig. 3.1, the plane $z = z_h$ is the measurement plane and is also called *hologram plane*, the plane $z = z_s$ corresponds to the surface of the vibrating plate. The acoustic pressure field, measured on the hologram plane, from a theoretical point of view is a continuous function, spanning the entire plane. Rayleigh's integrals, presented in Sec. 2.3, provide the pressure radiated from the source starting from the pressure or the normal velocity

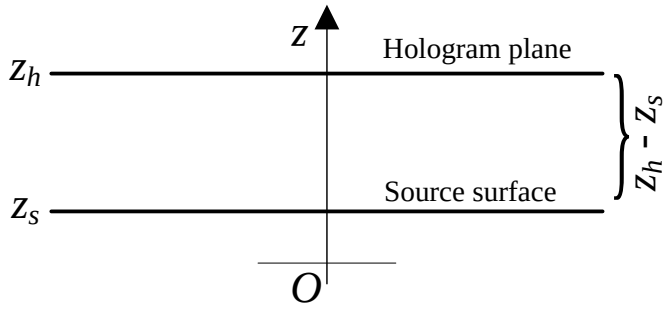

Figure 3.1: Hologram plane.

on planar surface. Acoustic holography, appeared in the 1960s and mother of NAH, and NAH aim at solving the inverse problem, that is reconstructing the surface velocity field on a plate from the measurement of the acoustic pressure field on the hologram plane close to the plate. Acoustic holography back-propagates the pressure field towards the source. Since the pressure field is recorded many wavelengths away from the source, acoustic holography can reconstruct only source spatial details greater than the acoustic wavelength since the solution is only an approximation to the inverse problem. Twenty years later, in the 1980s, Williams and Maynard proposed the NAH [7] which provides a rigorous solution to the inverse problem. In order to increase the resolution of the reconstructed surface velocity field, a fundamental requirement is that of measuring the sound field near the sources: in this way it is possible to acquire also the evanescent waves. For this reason the prefix *nearfield* was added. Evanescent waves are very important because they allow us to reconstruct high frequency spatial details and thus overcome the wavelength resolution limit [8].

Combining the Euler's equation (2.20) and the expression of the angular spectrum, Eq. (2.24), we obtain the angular spectrum of the normal velocity as

$$V_n(k_x, k_y, z) = \frac{k_z}{\rho_0 ck} e^{jk_z(z-z_h)} P(k_x, k_y, z_h) = G(k_x, k_y, z - z_h) P(k_x, k_y, z_h), \tag{3.1}$$

where

$$G(k_x, k_y, z - z_h) \equiv \frac{k_z}{\rho_0 ck} e^{jk_z(z-z_h)} \tag{3.2}$$

is the velocity propagator [1]. Now we can find the normal velocity on the plate as

$$v_n(x, y, z_s) = \mathcal{F}_x^{-1}\mathcal{F}_y^{-1}[\mathcal{F}_x\mathcal{F}_y[p(x, y, z_h)]G(k_x, k_y, z_s - z_h)], \tag{3.3}$$

where $\mathcal{F}_x\mathcal{F}_y[\cdot]$ and $\mathcal{F}_x^{-1}\mathcal{F}_y^{-1}[\cdot]$ represent respectively the 2D Fourier transform and the 2D inverse Fourier transform and $p(x, y, z_h)$ is the pressure measured on the hologram plane. Using the convolution theorem Eq. (3.3) can be rewritten as

$$v_n(x, y, z_s) = p(x, y, z_h) * *g_v^{-1}(x, y, z_s - z_h), \tag{3.4}$$

where $(**)$ represents a 2D convolution and the inverse propagator is defined as

$$\begin{aligned} g_v^{-1}(x, y, z_s - z_h) \equiv \mathcal{F}_x^{-1}\mathcal{F}_y^{-1}[G(k_x, k_y, z_s - z_h)] = \\ \mathcal{F}_x^{-1}\mathcal{F}_y^{-1}[\frac{k_z}{\rho_0 ck} e^{jk_z(z_s-z_h)}]. \end{aligned} \tag{3.5}$$

NAH aims at solving an inverse problem so we must ensure that the solution is unique and stable. The first problem encountered is due to the velocity propagator G defined in Eq. (3.2). Recalling the dispersion relation, Eq. (2.7), we can define $k_z = \sqrt{k^2 - k_x^2 - k_y^2}$ if k_x^2 and k_y^2 are greater than zero and $k_z = j\sqrt{k_x^2 + k_y^2 - k^2} = jk_z'$ if k_x^2 and k_y^2 are less than zero. In the second case we have evanescent waves so we are in presence of an exponentially decaying sound field. Rewriting the exponential at the right-hand member of Eq. (3.2) we obtain

$$e^{-jk_z(z_h - z_s)} = e^{k_z'(z_h - z_s)}. \tag{3.6}$$

When k_x and k_y tend to infinity the inverse propagator, which multiplies the angular spectrum $P(k_x, k_y, z_h)$ of the pressure measured on the hologram plane, also tends to infinite. In order to have the product $G(k_x, k_y, z_s - z_h)P(k_x, k_y, z_h)$ finite we must assume that the pressure angular spectrum drops off faster if compared with the rising rate of the propagator. This is ideally true since the evanescent waves angular spectrum is defined as

$$P(k_x, k_y, z_h) = P(k_x, k_y, z_s)e^{-k_z'(z_h - z_s)}. \tag{3.7}$$

The exponential decay in Eq. (3.7) and the exponential growth in Eq (3.2) cancel each other out. In the real world the presence of noise in measurements and numerical approximations completely destroys the cancellation process.

To overcome this problem we have to limit the angular spectrum, reducing the high wavenumber content, by means of a filter [1]. We have to limit the angular spectrum since the square modulus of the velocity propagator

$$|G(k_x, k_y, z_s - z_h)|^2 = \begin{cases} (k_z/\rho_0 ck)^2 & k_x^2 + k_y^2 \leq k^2 \\ (k_z'/\rho_0 ck)^2 e^{2k_z'(z_h - z_s)} & k_x^2 + k_y^2 > k^2 \end{cases} \tag{3.8}$$

grows without bound as the wavenumbers increase.

We can express the insertion of the filter in a symbolic form as

$$\tilde{P}(k_x, k_y, z_h)\Pi[k_x/(2k_{c_x}), k_y/(2k_{c_y})]G(k_x, k_y, z_s - z_h), \tag{3.9}$$

where Π is a 2D rectangle window with cutoff at $k_x = k_{c_x}$ and $k_y = k_{c_y}$ respectively. The term $\tilde{P}(k_x, k_y, z_h)$ is the noisy angular spectrum defined by

$$\tilde{P}(k_x, k_y, z_h) = P(k_x, k_y, z_h) + \mathcal{N}(k_x, k_y), \tag{3.10}$$

where $\mathcal{N}(k_x, k_y) = \mathcal{F}_x\mathcal{F}_y[\epsilon(x, y)]$ and $\epsilon(x, y)$ represent uncorrelated spatial noise.

The introduction of the filter is crucial to limit the wavenumbers (k_x, k_y) and thus to avoid that G grows to infinte. The downside is due to the fact that the inverse Fourier transform of a 2D rectangular window is a 2D *sinc* function.

The sinc function (cardinal sine function), denoted by $\mathrm{sinc}(x)$ is defined by

$$\begin{cases} \mathrm{sinc}(x) = \frac{\sin(x)}{x} & \text{for } x \neq 0 \\ \mathrm{sinc}(x) = 1 & \text{for } x = 0, \end{cases} \tag{3.11}$$

where $x \in \mathbb{R}$. The normalized sinc function, commonly used in digital signal processing, is defined by

$$\begin{cases} \mathrm{sinc}(x) = \frac{\sin(\pi x)}{\pi x} & \text{for } x \neq 0 \\ \mathrm{sinc}(x) = 1 & \text{for } x = 0. \end{cases} \tag{3.12}$$

The 2D sinc function is defined by the product of two 1D sinc functions

$$\mathrm{sinc}(x, y) = \mathrm{sinc}(x)\,\mathrm{sinc}(y), \tag{3.13}$$

where $(x, y) \in \mathbb{R}^2$.

In the time domain the sinc function is convolved with the desired solution and thus we cannot reconstruct correctly the velocity v_n. Furthermore the spatial filter Π eliminates all wavenumbers above (k_{c_x}, k_{c_y}) which are the cutoff coefficients. The cutoff coefficients correspond to the spatial wavelengths $(\lambda_{c_x}, \lambda_{c_y}) = (2\pi/k_{c_x}, 2\pi/k_{c_y})$ therefore spatial details of the vibrating object less than $(\lambda_{c_x}/2, \lambda_{c_y}/2)$ cannot be reconstructed. The choice of the values (k_{c_x}, k_{c_y}) is very important and they have to be chosen so that the 2D rectangular window contains the most of the wavenumber of the source.

Some problems, due to the rectangular window filter, can be reduced using a tapered window with smooth cutoff [1]. The window is modified as

$$\hat{\Pi}(k_x/(2k_{c_x}), k_y/(2k_{c_y})) = \hat{\Pi}(k_x/(2k_{c_x})\hat{\Pi}(k_y/(2k_{c_y}) \tag{3.14}$$

where

$$\hat{\Pi}(k_x/(2k_{c_x})) = \begin{cases} 1 - \frac{1}{2}e^{-(1-|k_x|/k_{c_x})/\beta} & |k_x| < k_{c_x} \\ \frac{1}{2}e^{(1-|k_x|/k_{c_x})/\beta} & |k_y| > k_{c_y} \end{cases} \tag{3.15a}$$

$$\hat{\Pi}(k_y/(2k_{c_y})) = \begin{cases} 1 - \frac{1}{2}e^{-(1-|k_y|/k_{c_y})/\beta} & |k_y| < k_{c_y} \\ \frac{1}{2}e^{(1-|k_y|/k_{c_y})/\beta} & |k_y| > k_{c_y} \end{cases} \tag{3.15b}$$

the parameter β controls the decay rate of the window. If β tends to zero the 2D window coincides with the 2D rectangular window.

Another important aspect related to the choice of the cutoff coefficients is the standoff distance, $z_h - z_s$, and the signal-to-noise ratio of the pressure measured at the hologram plane. Let the signal-to-noise ratio (SNR) of the measurement system be expressed in decibels. If we want to measure the evanescent component k_{c_x} we must guarantee that

$$10^{\mathrm{SNR}/20} > e^{k_{c_x}(z_h - z_s)}. \tag{3.16}$$

If we consider now the spatial resolution $R_x = \lambda_{c_x}/2$ we obtain

$$R_x = 20\pi(z_h - z_s)\log(e)/\mathrm{SNR}. \tag{3.17}$$

In an analogous way we can derive the spatial resolution in the y-direction. The above equation highlights the fact that the spatial resolution depends on the standoff distance and the SNR.

The last problem is related to the fact that the acoustic pressure field cannot be acquired on the whole holographic plane $z = z_h$ and in a continuous way. The limited area of the holographic plane over which the measurements are made is called measurement aperture. This problem still exists with other techniques. We can express the effect of the measurement aperture by means of a 2D rectangular window of length W_x and width W_y. The Eq. (3.3) becomes

$$\begin{aligned}&\hat{v}_n(x, y, z_s) = \\ &\mathcal{F}_x^{-1}\mathcal{F}_y^{-1}[\mathcal{F}_x\mathcal{F}_y[p(x, y, z_h)\Pi(x/W_x)\Pi(y/W_y)]G(k_x, k_y, z_s - z_h)],\end{aligned} \tag{3.18}$$

where $\hat{\cdot}$ indicates that $\hat{v}_n$ differs from v_n due to the finite measurement aperture. The effect of the finite measurement aperture is clearly visible if we consider the angular spectrum of the measured pressure

$$\begin{aligned}&\mathcal{F}_x\mathcal{F}_y[p(x, y, z_h)\Pi(x/W_x)\Pi(y/W_y)] = \\ &\qquad P(k_x, k_y, z_h) * *W_x W y \,\mathrm{sinc}(k_x W_x/2)\,\mathrm{sinc}(k_y W_y/2).\end{aligned} \tag{3.19}$$

The angular spectrum is modified due to the convolutions with the two sinc functions. When the dimensions of the measurement aperture, W_x and W_y, tend to infinity the sinc functions tend to delta functions and the spread of the angular spectrum P goes to zero.

Finding a closed form expression for the error introduced in Eq. (3.18) from the finite measurement aperture is very difficult. However, the experience with NAH over the years, has highlighted that the measurement aperture must always be larger than the source plate. In the worst case the dimension of the measurement aperture must be chosen to be double the size

of the source plate. This makes that the pressure field drops off significantly towards the edge of the aperture. Recalling the simply supported plate example, presented in Sec. 2.3.1, the measurement aperture dimensions have to be chosen as $W_x = 2L_x$ and $W_y = 2L_y$.

Up to now the acoustic pressure field and the velocity field have been considered continuous in the spatial domain. From a practical point of view this is not possible and therefore the pressure and velocity fields are spatially sampled. The microphones, usually, are positioned on a regular grid with finite steps Δx and Δy along x and y directions, respectively. The spatial sampling process can be represented using the *comb* function.

The comb function (*Dirac* comb) is defined by

$$\text{Ш}_X(x) \stackrel{def}{=} \sum_{m=-\infty}^{\infty} \delta(x - mX) = \frac{1}{X}\,\text{Ш}(\frac{x}{X}), \tag{3.20}$$

where X is the period.

Considering, for simplicity, the 1D Fourier transform we can write the angular spectrum of the sampled acoustic pressure field as

$$\tilde{P}(k_x) = \int_{-\infty}^{\infty} p(x)\,\text{Ш}(x/\Delta x)e^{-jk_x x}dx = \Delta x/2\pi P(k_x) * \text{Ш}(\frac{k_x}{2\pi/a}), \tag{3.21}$$

where $P(k_x)$ is the angular spectrum of the continuous pressure field and $\tilde{P}(k_x)$ is the angular spectrum of the sampled pressure field. Using the definition of comb function we can rewrite the Eq. (3.21) as

$$\tilde{P}(k_x) = \sum_{m=-\infty}^{\infty} P(k_x - \frac{2\pi m}{\Delta x}). \tag{3.22}$$

The last equation is the mathematical definition of the *aliasing*. The right-hand member of Eq. (3.22) is the sum of the replicas of the exact transform of the continuous pressure field, each shifted by $2\pi/\Delta x$. If the original angular spectrum is not band limited in k_x then the part of $P(k_x)$ with $|k_x| > 2\pi/\Delta x$ will overlap the nearby replicas ($m \pm 1$). In a similar way the replicas $P(k_x \pm 2\pi/\Delta x)$ will overlap $P(k_x)$, degrading the wanted transform. The discretization of the holography equation (3.3), needing to deal with it in the real world, leads to the discrete Fourier transform (DFT) and fast Fourier transform (FFT) algorithms. The Eq. (3.3) can be rewritten as

$$v_{\mathcal{D}_n}(x, y, z_s) = \mathcal{D}_x^{-1}\mathcal{D}_y^{-1}[\mathcal{D}_x\mathcal{D}_y[p(x, y, z_h)]G(k_x, k_y, z_s - z_h)], \tag{3.23}$$

where $\mathcal{D}_x\mathcal{D}_y[\cdot]$ and $\mathcal{D}_x^{-1}\mathcal{D}_y^{-1}[\cdot]$ represent the 2D DFT and 2D inverse DFT operators, and the subscript $_{\mathcal{D}}$ represents the use of the DFT. The 1D DFT

is defined by

$$\mathcal{D}_x[p(x)] \equiv P_{\mathcal{D}}(n\Delta k_x) = \Delta x \sum_{m=-N/2}^{N/2-1} p(m\Delta x) e^{-2\pi jnm/N}, \tag{3.24}$$

where $N = W_x/\Delta x$, Δx is the spatial sampling step (N samples), while $k_x = n\Delta k_x = n(2\pi/W_x)$ and Δk_x represents the smallest spatial frequency that can be resolved. Now, the 1D pressure angular spectrum, computed by means of the DFT, can be derived starting from

$$P_{\mathcal{D}}(k_x) \equiv \int_{-\infty}^{\infty} p(x)\, \text{Ш}(x/\Delta x)\Pi(x/W_x) e^{-jk_x x} dx, \tag{3.25}$$

which leads to the DFT

$$P_{\mathcal{D}}(n\Delta k_x) = \Delta x \sum_{m=-N/2}^{N/2-1} p(m\Delta x) e^{-2\pi jnm/N}. \tag{3.26}$$

Now, we can write, symbolically, the 2D case

$$\begin{aligned} &\mathcal{D}_x^{-1}\mathcal{D}_y^{-1}[P_{\mathcal{D}}(k_x, k_y, z_h)] = \\ &\mathcal{F}_x^{-1}\mathcal{F}_y^{-1}[P_{\mathcal{D}}(k_x, k_y, z_h)\, \text{Ш}(\frac{k_x}{\Delta k_x})\, \text{Ш}(\frac{k_y}{\Delta k_y})\Pi(\frac{k_x}{\Delta 2k_m})\Pi(\frac{k_y}{\Delta 2k_m})], \end{aligned} \tag{3.27}$$

where $k_m \equiv \pi/a$ is the maximum wave number and $a = \Delta x = \Delta y$, $\Delta k_x = 2\pi/W_x$ and $\Delta k_y = 2\pi/W_y$. Combining Eq. (3.23) and Eq. (3.27) we can write the DFT version of the holographic reconstruction equation

$$\begin{aligned} v_{\mathcal{D}_n}(x, y, z_s) =& \mathcal{F}_x^{-1}\mathcal{F}_y^{-1}[P_{\mathcal{D}}(k_x, k_y, z_h) G(k_x, k_y, z_s - z_h) \\ &\times \text{Ш}(\frac{k_x}{\Delta k_x})\, \text{Ш}(\frac{k_y}{\Delta k_y})\Pi(\frac{k_x}{\Delta 2k_m})\Pi(\frac{k_y}{\Delta 2k_m})]. \end{aligned} \tag{3.28}$$

Thanks to the convolution theorem we can rewrite Eq. (3.28) as

$$\begin{aligned} v_{\mathcal{D}_n}(x, y, z_s) =& p_{\mathcal{D}}(x, y, z_h) ** \frac{1}{W_x W_y}\, \text{Ш}(\frac{x}{W_x}, \frac{y}{W_y}) \\ &** \mathcal{F}_x^{-1}\mathcal{F}_y^{-1}[G] ** \frac{1}{\Delta x \Delta y}\, \text{sinc}(\frac{\pi x}{\Delta x})\, \text{sinc}(\frac{\pi y}{\Delta y}), \end{aligned} \tag{3.29}$$

where $p_{\mathcal{D}}(x, y, z_h)$ is the inverse (continuous) Fourier transform of $P_{\mathcal{D}}$ defined as

$$p_{\mathcal{D}}(x, y, z_h) = p(x, y, z_h)\, \text{Ш}(x/\Delta x, y/\Delta y)\Pi(x/W_x, y/W_y). \tag{3.30}$$

The last equation highlights that $p_{\mathcal{D}}$ is a sampled version of the measured pressure over the measurement amplitude. To prevent spatial aliasing we

must assert that the highest spatial wavenumbers containing significant energy must be sampled at least at the rate of two samples per wavelength as established by the sampling theorem.

The effect of the convolution with the two sinc functions in Eq. (3.29) can be neglected since the width of the main lobe of the sinc functions spans only two sample points. The 2D comb function is a series of impulses at distance W_x and W_y in the x and y direction and the 2D convolution with the function $p_{\mathcal{D}}(x, y, z_h)$ in Eq. (3.29) becomes

$$p_{\mathcal{D}}(x, y, z_h) ** \frac{1}{W_x W_y} \amalg\left(\frac{x}{W_x}, \frac{y}{W_y}\right) = \sum_{m,n=-\infty}^{\infty} p_{\mathcal{D}}(x - mW_x, y - nW_y). \quad (3.31)$$

The right hand member of the last equation, is the summation of the infinite replicas of the measurement aperture, shifted in space. The term which corresponds to $(m, n) = (0, 0)$ is the original measurement aperture. To reduce the error due to the replicated measurement apertures is common practice to zero-padding the original measurements. This leads to an increased separation between the replicated measurements. The final result is therefore expressed by

$$\tilde{v}_{\mathcal{D}_n}(x, y, z_s) = \sum_{m,n=-\infty}^{\infty} p_{\mathcal{D}}(x - mW_x, y - nW_y, z_h) * * \mathcal{F}_x^{-1}\mathcal{F}_y^{-1}[G]. \quad (3.32)$$

Discussion

The classical implementation of NAH is a simple tool to deal with planar geometries. Its implementation is very fast since it is based on the DFT and FFT algorithms. This method can be improved, for example exploiting some a-priori knowledge as we will see in the following section, to reduce the number of measurement points or to improve the robustness in presence of noisy measurements.

3.2 Planar Near-field acoustic holography based on compressive sensing

To improve the performances of the classical Planar NAH implementation various studies have been conducted. An interesting case is the one proposed by Chardon, Daudet *et al* which exploits a sparse domain framework and uses a compressive sensing approach to solve the NAH problem [2].

The method proposed by Chardon, Daudet *et al* aims at exploiting the fact that the normal velocity of a plate, when expressed in a proper basis,

is sparse. The main idea is to approximate the velocity as a sum of few elementary, well known, analytical basis function. This method can be applied on convex homogeneous plates with arbitrary boundary conditions and can handle velocity field discontinuities at the boundary. The technique also aims at reducing the number of measurements needed (i.e. microphones) taking advantages of the concept of compressive sensing.

First of all the authors introduce the concept of sparsity. A signal can be defined sparse if it can be decomposed as linear combination of a small number of pre-defined functions. This functions are called atoms and are collected in a set $\mathcal{D}$, called *dictionary*. Assuming that the dictionary has size M and atoms $\mathbf{d}_k \in \mathbb{R}^N$ we can write $\mathcal{D} = \{\mathbf{d}_k\}_{k=1\dots M}$. If $M = N$ the dictionary will be a basis of $\mathbb{R}^N$, if $M > N$ it will be an over complete family spanning $\mathbb{R}^N$.

Let $\mathbf{s} \in \mathbb{R}^N$ a discrete signal. The signal can be defined sparse in $\mathcal{D}$ if there exists a set of coefficients γ_u such that

$$\mathbf{s} = \sum_{u \in U} \gamma_u \mathbf{d}_u, \tag{3.33}$$

where U is a subset of $\{1 \dots M\}$ and its cardinality $\#U \ll M$.

Applying this concept on NAH we can write the velocity field in the Fourier domain as

$$\mathbf{v} \approx \mathbf{D}\boldsymbol{\gamma}. \tag{3.34}$$

where $\mathbf{D} \in \mathbb{R}^{N \times M}$ is a matrix whose columns are the vector $\mathbf{d}_k$ in $\mathcal{D}$. The vector $\boldsymbol{\gamma} \in \mathbb{R}^{M \times 1}$, if we had used an appropriate basis, has only $\#U$ non-zero elements.

Now, to solve the inverse problem of NAH we have to find the few coefficient of the vector $\boldsymbol{\gamma}$ such that $\mathbf{p}_h = \mathbf{HD}\boldsymbol{\gamma}$ is valid, where $\mathbf{p}_h$ is the acoustic pressure measured on the hologram plane. The matrix $\mathbf{H}$ is defined as $\mathbf{F}^{-1}\mathbf{GF}$ where $\mathbf{G}$ is diagonal matrix, whose elements are equal to the Green's functions and $\mathbf{F}$ is the 2D spatial DFT operator. The 2D DFT, of a signal $\mathbf{X}$, can be expressed in matrix form as $\mathbf{FXF}^T$, where the DFT operator is defined as

$$[\mathbf{F}]_{a,b} = \frac{\chi^{ab}}{\sqrt{K}}, \tag{3.35}$$

where $\chi = e^{-\frac{2\pi j}{K}}$, K is the length of the DFT and with $[\cdot]_{a,b}$ we denote the element (a, b) of the the matrix $\mathbf{F}$ and a,b = 0,. . . ,K-1.

Introducing the ℓ_0 "norm" [1] of the vector $\boldsymbol{\gamma}$ the problem becomes

$$\arg\min_{\boldsymbol{\gamma}} \|\boldsymbol{\gamma}\|_0 \qquad \text{subject to} \qquad \mathbf{p}_h = \mathbf{H}\mathbf{D}\boldsymbol{\gamma}. \tag{3.36}$$

where $\|\boldsymbol{\gamma}\|_0 = \#U$. With the ℓ_0 "norm" the problem is non convex so we have to replace it with the ℓ_1 norm [1]. The problem becomes

$$\arg\min_{\boldsymbol{\gamma}} \|\boldsymbol{\gamma}\|_1 \qquad \text{subject to} \qquad \mathbf{p}_h = \mathbf{H}\mathbf{D}\boldsymbol{\gamma}. \tag{3.37}$$

This approach is called Basis Pursuit [9]. In presence of measurement noise we have to introduce a fidelity constrain ε, the problem turns to be

$$\arg\min_{\boldsymbol{\gamma}} \|\boldsymbol{\gamma}\|_1 \qquad \text{subject to} \qquad \|\mathbf{p}_h - \mathbf{H}\mathbf{D}\boldsymbol{\gamma}\|_2^2 \leq \varepsilon \tag{3.38}$$

and is called sparse ℓ_1 regularization. The choice of the tuning parameter ε is crucial: larger values of ε give a sparser solution $\boldsymbol{\gamma}$, but also a worst accuracy in the reconstruction.

Finally, rewriting Eq. (3.38) in a Lagrangian form we obtain the Basis Pursuit Denoising (BPDN) optimization problem

$$\arg\min_{\boldsymbol{\gamma}} \|\mathbf{p}_h - \mathbf{H}\mathbf{D}\boldsymbol{\gamma}\|_2^2 + \lambda\|\boldsymbol{\gamma}\|_1, \tag{3.39}$$

where λ is the tuning parameter. Comparing the BPDN approach with the classical Tikhonov regularization [10] the main difference is the choice of the norm: Tikhonov uses a ℓ_2 norm [1] for the vector $\boldsymbol{\gamma}$ while the BPDN uses a ℓ_1 norm. The BPDN promotes sparsity. In order to solve the problem in Eq. (3.39) we have first to build the dictionary $\mathbf{D}$. As seen in Chapter 2, a solution to the Helmholtz equation, Eq. (2.4), is given by plane wave. The plate velocity can be computed by the Kirchhoff-Love equation [11] and its solution can be approximated as a sum of plane and evanescent waves

$$\mathbf{v}(x,y) \approx \left(\sum_n \gamma_n e^{\jmath \mathbf{k}_n \cdot \mathbf{x}} + \zeta_n e^{\mathbf{k}_n \cdot \mathbf{x}} \right) \mathbf{1}_{\mathcal{S}}(x,y), \tag{3.40}$$

where $\mathbf{1}_{\mathcal{S}}(x,y)$ is a function that restricts the domain $\mathcal{S}$ of the plate. This approximation is valid for any *star-shape* [2] planar plate geometries. In this case the evanescent part is not crucial and therefore can be neglected. The

[1] Let $\mathbf{x} \in \mathbb{R}^N$. The ℓ_0 "norm" is defined as $\|\mathbf{x}\|_0 = \sum_n |x_n|^0$ with $0^0 \stackrel{def}{=} 0$. The ℓ_p norm is defined as $\|\mathbf{x}\|_p = \left(\sum_n |x_n|^p\right)^{\frac{1}{p}}$ for $p > 0$.

[2] A star-shaped plate is a plate in which exists a point that can be connected to any other point via a line segment that is entirely included in the plate.

choice of the dictionary domain dimension $\bar{\mathcal{S}}$ is the main degree of freedom in the design of the dictionary. If we consider a rectangular domain we can relate the dimensions D_x and D_y with the wavevectors k_x and k_y by $D_x = 2\pi/k_x$ and $D_y = 2\pi/k_y$. To obtain a finer resolution, or equivalently a better approximation, D_x and D_y must have larger dimensions. However, this increases the complexity of the problem raising the numerical dimension. The authors suggest to choose the domain $\bar{\mathcal{S}}$ twice the size of $\mathcal{S}$. In the rectangular plate case we have to choose $D_x = 2L_x$ and $D_y = 2L_y$.

Discussion

This method is more efficient than the classical NAH method described in Sec. 3.1, since it uses not only experimental data, but exploits a-priori knowledge based on the plane wave approximation of the Kirchhoff-Love equation solution. This approximation is valid only for star-shape planar plate geometries therefore this method cannot be adopted for more complex surfaces (e.g., curved ones such as that of the violin top plate).

3.3 Near-field acoustic holography based on Inverse BEM

To extend the NAH to complex geometries we have to consider more sophisticated methods. The first method we examine is the Inverse Boundary Element Method (iBEM) [3]. This method is based on the Boundary Element Method (BEM), a technique that allows us to predict the pressure field generated from an arbitrary vibrating source.

This method is based on the discretization of the Kirchhoff-Helmholtz integral equation, (2.19). The formulation of the Kirchhoff-Helmholtz integral in Eq. (2.19) is valid if the evaluation point is outside of the surface ∂V_0 of the object of interest. To derive the BEM formulation we have to consider a more general case in which the evaluation point $\mathbf{r}$ could be placed also on the surface ∂V_0, we have to slightly change the Eq. (2.19) as

$$\alpha P(\mathbf{r},\omega) = \oint_{\partial V} \left(\frac{\partial}{\partial \mathbf{n}} G(\mathbf{r}|\mathbf{r}',\omega) P(\mathbf{r}',\omega) - G(\mathbf{r}|\mathbf{r}',\omega) \frac{\partial}{\partial \mathbf{n}} P(\mathbf{r}',\omega) \right) d\mathbf{r}'. \tag{3.41}$$

where the parameter α is defined as

$$\begin{cases} \alpha = \frac{1}{2} & \text{for } \mathbf{r} \text{ on } \partial V_0, \\ \alpha = 1 & \text{for } \mathbf{r} \text{ outside } \partial V_0 \end{cases} \tag{3.42}$$

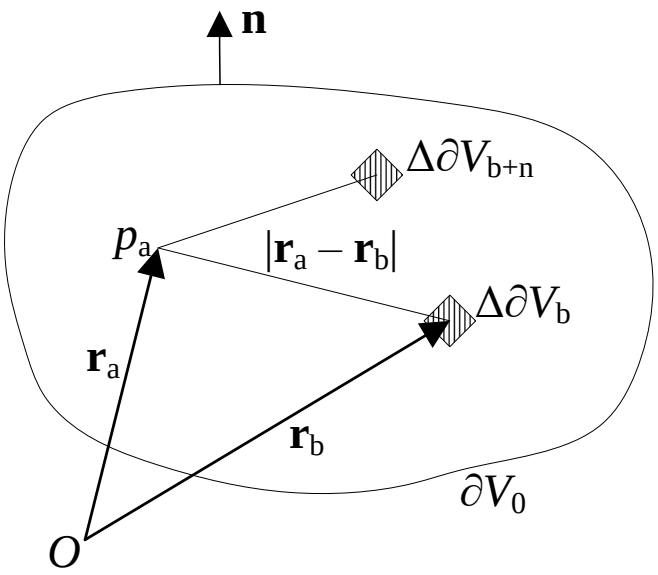

Figure 3.2: Discretization of the Kirchhoff-Helmholtz integral. 3D surface ∂V_0 divided into N elementes of area, $\Delta\partial V_n$.

If we consider discrete source points, as depicted in Fig. 3.2, the surface ∂V_0 is split into N small elements of area $\Delta\partial V_1, \Delta\partial V_2, \ldots, \Delta\partial V_N$. We consider also M discrete field points. The vector $\mathbf{r}_a$ is the position vector of the evaluation point and the vector $\mathbf{r}_b$ is the position vector of nth source element. Considering the evaluation point lies on the source surface ($\alpha = 1/2$), assuming that each element ∂V_n is small enough, we can approximate the Eq. (3.41) as

$$\frac{1}{2}p_a = \sum_{b=1}^{N}\left(p_b\frac{\partial G_{ab}}{\partial n} - G_{ab}\frac{\partial p_b}{\partial n}\right)\Delta\partial V_b, \tag{3.43}$$

where the subscripts a and b refer to the nth element of the surface. If we evaluate the Eq. (3.43) at every element of the surface we have N equations to solve for N values of p and N values of $\frac{\partial p}{\partial n}$.

Defining the $N \times N$ matrices

$$[\mathbf{G}_s]_{a,b} \equiv G_{ab} = \frac{e^{jk|\mathbf{r}_a - \mathbf{r}_b|}}{4\pi|\mathbf{r}_a - \mathbf{r}_b|} \tag{3.44}$$

and

$$[\mathbf{G}_{sv}]_{a,b} \equiv \frac{\partial G_{ab}}{\partial n} = \frac{\partial}{\partial n}\left(\frac{e^{jk|\mathbf{r}_a - \mathbf{r}_b|}}{4\pi|\mathbf{r}_a - \mathbf{r}_b|}\right), \tag{3.45}$$

$(a, b = 1, \ldots, N)$ which descretize the Green's function and its partial derivative respect to the normal direction, we can express the Eq. (3.43) in matrix

form as

$$\frac{1}{2}\mathbf{p}_s = \left(\mathbf{G}_{sv}\mathbf{S}\mathbf{p}_s - \mathbf{G}_s\mathbf{S}\frac{\partial \mathbf{p}_s}{\partial n}\right), \tag{3.46}$$

where $\mathbf{p}_s$ is the vector which describes the acoustic pressure field on the N elements of the surface. $\mathbf{S}$ is the discretized area matrix, a diagonal matrix whose elements are the N elements of area $\Delta\partial V_n$.

In an analogous way, if we consider the evaluation point outside the volume enclosed by the surface ∂V_0 ($\alpha = 1$), we can express the pressure as

$$\mathbf{p}_h = \left(\mathbf{G}_v\mathbf{S}\mathbf{p}_s - \mathbf{G}\mathbf{S}\frac{\partial \mathbf{p}_s}{\partial n}\right), \tag{3.47}$$

where $\mathbf{p}_h$ is the vector which describes the acoustic pressure field in the M points of measurement, in our case on the holographic plane. The matrices $\mathbf{G}$ and $\mathbf{G}_v$ are $M \times N$ matrices which descretize the Green's function and the relative partial derivative which relate the N points on the surface with the M measurement points.

Combining Eqs. (3.46) and (3.47) and by means of the Euler's equation (2.20), it is possible to compute the pressure field as

$$\mathbf{p}_h = j\rho_0 ck\left[\mathbf{G}_v\mathbf{S}\left(\mathbf{G}_{sv}\mathbf{S} - \frac{1}{2}\mathbf{I}\right)^{-1}\mathbf{G}_s\mathbf{S} - \mathbf{G}\mathbf{S}\right]\mathbf{v} = \mathbf{H}\mathbf{v}, \tag{3.48}$$

where $\mathbf{H}$ is the transfer matrix which includes geometric information on the system and relates the pressure field to the normal velocity of the source surface.

To solve the NAH problem we have to invert the Eq. (3.48). Generally the matrix $\mathbf{H}$ is non-square and has complex elements therefore to invert it we have to use a least-squared method and singular value decomposition (SVD). The SVD of the transfer matrix is given by

$$\mathbf{H} = \mathbf{U}\mathbf{\Sigma}\mathbf{V}^H, \tag{3.49}$$

where $\mathbf{\Sigma} = \mathrm{diag}(\sigma_1, \sigma_{2,\ldots}, \sigma_n)$ and ^{H} indicates the *Hermitian transpose*. The elements of the matrix $\mathbf{\Sigma}$ are the singular values. By means of the SVD we can invert the Eq. (3.48) as

$$\mathbf{v} = \mathbf{H}^\dagger\mathbf{p}_h = \mathbf{V}\mathbf{\Sigma}^{-\mathbf{1}}\mathbf{U}^H\mathbf{p}_h, \tag{3.50}$$

where † denotes the pseudo-inverse matrix of $\mathbf{H} \in \mathbb{C}^{M\times N}$. M is the number of points in which the field pressure is known and N is the number of points where we want to compute the normal velocity.

Due to the nature of the problem and the measurement noise the transfer matrix $\mathbf{H}$ is ill-conditioned and its condition number is high. If we directly invert the matrix $\mathbf{H}$ the evanescent wave components will be amplified by high-order singular values. To overcome this problem we can use a low-pass filter, such as Wiener filter or we can use an iterative inverse solution combined with a regularization technique.

A common technique is the Tikhonov regularization [10] together with the L-curve [12] criterion to determine the optimal Tikhonov parameter. The problem can be written in this form

$$\arg\min_{\mathbf{v}} \|\mathbf{H}\mathbf{v} - \mathbf{p}_h\|_2^2 + \lambda^2 \|\mathbf{I}\mathbf{v}\|_2^2, \tag{3.51}$$

where λ is the tuning parameter to control the weight of $\|\mathbf{I}\mathbf{v}\|_2^2$ in the minimization process. $\mathbf{I}$ is the identity matrix. The matrix $\mathbf{\Gamma} = \lambda\mathbf{I}$ is called Tikhonov matrix.

Discussion

As we have seen the iBEM is a method that can be used to back-propagate the sound field, starting from the pressure measured on a surface, very close to the source, to retrieve the normal velocity of the source itself. It works with complex geometries but its computational complexity grows rapidly with the number of points, N, used to approximate the source geometry and the number of measurement points M. This is clearly visible from the fact that we have to compute four matrices, $\mathbf{G}_s$, $\mathbf{G}_{sv}$, $\mathbf{G}$, $\mathbf{G}_v$, to solve the problem via numerical approximation. The first two matrices have dimension $N \times N$, while the second two have dimension $M \times N$, generally $M \ll N$. Moreover we have to compute the matrix $\mathbf{S}$ of size $N \times N$. The number of measurement points are in the order of a hundred, the points used to approximate the source instead are in the order of thousands therefore these matrices may be very large.

3.4 Near-field acoustic holography based on Equivalent Source Method

The Equivalent Source Method (ESM) is a technique which has been developed to overcome the problems related to the numerical complexity of the BEM. The ESM, instead of computing directly the acoustic pressure starting from the normal velocity on the surface, introduces a further step. The ESM models the acoustic pressure generated by a vibrating source as the sound

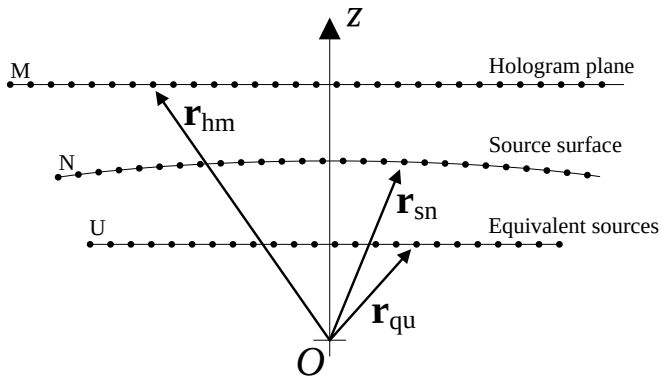

Figure 3.3: Positioning of the M measurement points and U equivalent sources respect to the N points source surface.

field obtained superposing the effect of a set of equivalent virtual sources located within the source itself. The ESM operates in two steps. The first step involves the solution of an inverse problem to find the strength (complex weights) of the equivalent sources starting from the normal velocity of the vibrating object surface. Then, a suitable propagator function is applied to the equivalent sources, in order to compute the acoustic pressure field on the measurement plane.

The idea of Zhang, Jacobsen *et al* presented in [4] is to invert the ESM in such a way to compute the normal velocity of the source surface starting from the pressure measurements to perform NAH. Also this method is based on the Kirchhoff-Helmholtz integral equation, (2.19). The equivalent sources are positioned on a regular grid below the source surface. Given M measurement points on the hologram plane and U equivalent sources, as illustrated in Fig. 3.3, the pressure on the hologram plane can be expressed in matrix form as

$$\mathbf{p}_h = j\rho_0 ck\mathbf{G}_{hp}\mathbf{q}, \tag{3.52}$$

where $\mathbf{q} = [q(\mathbf{r}_{q1}), q(\mathbf{r}_{q2}), \ldots, q(\mathbf{r}_{qU})]^T$ is the column vector which includes the N equivalent source weights $q(\mathbf{r}_{qu})$ and $\mathbf{r}_{qu}$ is the position vector of the uth source. The matrix $\mathbf{G}_{hp}$ is the transfer matrix obtained from the free space Green's function, Eq. (2.15),

$$[\mathbf{G}_{hp}]_{mu} = G(\mathbf{r}_{hm}|\mathbf{r}_{qu}, \omega) = \frac{1}{4\pi}\frac{e^{-jk|\mathbf{r}_{hm}-\mathbf{r}_{qu}|}}{|\mathbf{r}_{hm}-\mathbf{r}_{qu}|}, \tag{3.53}$$

where $m = 1, \ldots, M$, $u = 1, \ldots, U$ and $\mathbf{r}_{hm}$ is the position of the mth point on the hologram plane.

The unknown equivalent source vector can be obtained as

$$\mathbf{q} = \frac{1}{j\rho_0 ck}\mathbf{G}_{hp}^{\dagger}\mathbf{p}_h, \tag{3.54}$$

where the matrix $\mathbf{G}_{hp}^{\dagger}$ is the Moore-Penrose pseudoinverse of the matrix (3.53) computed by means of the SVD. Now, it is possible to compute the surface pressure $\mathbf{p}_s$ or the normal velocity $\mathbf{v}$ as

$$\mathbf{p}_s = j\rho_0 ck\mathbf{G}_{sp}\mathbf{q}, \tag{3.55}$$

$$\mathbf{v} = \mathbf{G}_{sv}\mathbf{q}, \tag{3.56}$$

where $\mathbf{G}_{sp}$ and $\mathbf{G}_{sv}$ are the complex transfer matrices defined as

$$[\mathbf{G}_{sp}]_{nu} = G(\mathbf{r}_{sn}|\mathbf{r}_{qu},\omega) = \frac{1}{4\pi}\frac{e^{-jk|\mathbf{r}_{sn}-\mathbf{r}_{qu}|}}{|\mathbf{r}_{sn}-\mathbf{r}_{qu}|}, \tag{3.57}$$

$$[\mathbf{G}_{sv}]_{nu} = \frac{\partial}{\partial \mathbf{n}_s}G(\mathbf{r}_{sn}|\mathbf{r}_{qu},\omega) = \frac{\partial}{\partial \mathbf{n}_s}\left(\frac{1}{4\pi}\frac{e^{-jk|\mathbf{r}_{sn}-\mathbf{r}_{qu}|}}{|\mathbf{r}_{sn}-\mathbf{r}_{qu}|}\right), \tag{3.58}$$

where $n = 1,\ldots,N$, $\mathbf{r}_{sn}$ is the vector that identifies the position of the nth point on the source surface and $\mathbf{n}_s$ is the outward normal of the source.

Combining Eq. (3.54) with Eq. (3.56) it is possible to compute the normal velocity of the source with arbitrary geometry, starting from the pressure field measured on the hologram plane as

$$\mathbf{v} = \mathbf{G}_{sv}\mathbf{q} = \frac{1}{j\rho_0 ck}\mathbf{G}_{sv}\mathbf{G}_{hp}^{\dagger}\mathbf{p}_h. \tag{3.59}$$

Thanks to the equivalent sources the dimensionality of the problem, and in particular the size of the matrix to be inverted, is highly reduced with respect to the iBEM approach. For this reason, ESM turns to be more efficient from the computational point of view. More specifically, the dimensionality of the problem is governed by the number M of measurement points and the number U of considered equivalent sources. A typical choice is to set $U \approx M$. For this reason the matrix $\mathbf{G}_{hp} \in \mathbb{R}^{M\times U}$ has relatively small dimension and the inverse matrix $\mathbf{G}_{hp}^{\dagger}$ can be computed quite easily. Due to the nature of the problem, the matrix $\mathbf{G}_{hp}$ can be ill-conditioned and its condition number can be high. In this case the SVD method, used to invert the matrix, fails and we have to use another technique. As in the iBEM case, we have to use a regularization technique to perform the inversion correctly. The main techniques used are the Tikhonov regularization [10] combined with the L-curve method [12] or the truncated SVD (T-SVD) [13].

The main drawback of the ESM is related to measurement noise. If the pressure measurements are corrupted by noise it is not guaranteed that the equivalent source weights are computed correctly. If the equivalent source weights are not properly computed we cannot reconstruct the original source surface velocity. If we consider the measured pressure described as

$$\mathbf{p}_h = (\mathbf{p}_h)_r + (\mathbf{p}_h)_e, \tag{3.60}$$

where $(\cdot)_r$ represents the exact value and $(\cdot)_e$ represents the error component of the measured pressure respectively, we can write the reconstructed surface normal velocity as

$$\mathbf{v} = (\mathbf{v})_r + (\mathbf{v})_e = \frac{1}{j\rho_0 ck}\mathbf{G}_{sv}\mathbf{G}_{hp}^{\dagger}[(\mathbf{p}_h)_r + (\mathbf{p}_h)_e]. \tag{3.61}$$

The relative error upper bound can be computed as

$$\frac{\|(\mathbf{v})_e\|}{\|(\mathbf{v})_r\|} \leq \text{cond}(\mathbf{G}_{sv})\text{cond}(\mathbf{G}_{hp})\frac{\|(\mathbf{p}_h)_e\|}{\|(\mathbf{p}_h)_r\|}, \tag{3.62}$$

where $\|\cdot\|$ represents the vector norm and $\text{cond}(\cdot)$ is the condition number of a matrix. The Eq. (3.62) highlights that the error will be amplified by the condition numbers of the matrices $\mathbf{G}_{sv}$ and $\mathbf{G}_{hp}$.

Another critical point is the positioning of the equivalent sources since the accuracy of the method is related to it. The equivalent sources have to be positioned on a plane, under the source surface, relatively close to it. The distance between the plane of the equivalent sources and the source surface has to be approximatively equal to the distance between the source surface and the measurement plane [14]. The step of the grid, over which the equivalent sources are positioned, has to be slightly smaller to the step of the measurements grid [14]. This can be proved empirically considering the solid angle. Let A_h be the area covered by the measurement aperture plane and d_h its distance from the origin O of the coordinate system. Let $d_q < d_h$ the distance from the origin of the equivalent sources plane. If the solid angle Ω is constant the area cover by the equivalent sources A_q must be smaller than A_h since $\Omega = A_h/R_h^2 = A_q/R_q^2$.

Discussion

The iBEM requires the numerical discretization of integral equations, as discussed in Sec. 3.3, which can be an expensive technique when the number of reconstruction and measurement points is large. The matrix system required for the ESM based NAH is obtained by the evaluation of the Green's

function at the source points, and no boundary elements are used. If the measurement plane is close enough to the source surface, in such a way that the evanescent waves are captured properly, it can be demonstrated that the approximation error of the ESM based NAH is comparable with that of the iBEM [15]. The ESM therefore is a very efficient method and sufficiently accurate.

Chapter 4

Dictionary based ESM

As we have seen in Chapter 3 the ESM is a powerful technique which allows us to deal with complex geometries in an efficient way from a computational point of view. However, as described in Sec. 3.4, it cannot guarantee a perfect reconstruction of the source velocity if there are few measurements available and if a high level of noise is present. In Sec. 3.2 we have also seen that if we seek the solution in a sparse domain we can reduce the number of measurements required and also improve the performances in presence of measurements noise.

In this chapter we propose a novel method for NAH, which combines the flexibility of the ESM with the advantages of searching for the solution in a sparse domain. The proposed technique aims at being robust in those situations where it is not possible to use a great number of microphones and in presence of measurement noise or a certain amount of reverberation. It also aims at overcoming the frequency limits imposed by the spatial sampling theorem.

4.1 Methodology overview

With reference to the block diagram in Fig. 4.1 we illustrate the working principles of our method. Starting from the CAD model of the source, by means of FEA [16] we compute the *theoretical* normal velocity of the source vibrating surface imposing the physical parameters of the material taken from a large set of possible values, as we will illustrate in Sec. 4.2.

Back-propagating the normal velocity on the plane of the equivalent sources, which are previously positioned, we can compute their weights. As discuss in Sec. 4.3, this operation has to be done for each combination of parameters used in the previous step and for each mode of vibration

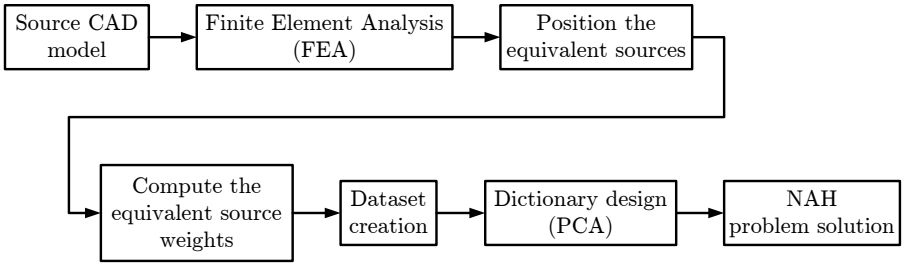

Figure 4.1: Block diagram of the working principle of the Dictionary based ESM

identified by FEA.

The equivalent source weights are collected in a dataset, grouped by mode index. Starting from the equivalent source weights in the dataset, by means of the Principal component analysis (PCA) [17], we compute the principal components for each mode. The principal components are the vectors which will be included in the dictionary.

Finally, we can estimate the *real* velocity of the source surface selecting from the dictionary the better linear combination of equivalent source weights according to the pressure measured on the hologram plane and then propagating the selected components on the source surface.

In the following sections, we will discuss in detail each aspect of the proposed methodology.

4.2 Finite element analysis

Finite Element Analysis (FEA), also known as Finite Element Method (FEM) [16], is a numerical method to solve partial differential equation problems. This technique allows us to reduce a differential equation to an algebraic equations system. The main characteristic of FEA is related to the discretization of the domain (the object we want to analyse) by means of finite elements of predefined shape. For each element the solution to the problem will be a linear combination of basis functions, also known as *shape functions*. An example of basis functions could be the polynomial functions and the solution to the problem could be approximated by a piece wise linear function.

Starting from the geometry of the source we can build a 3D CAD model. This model is called *mesh*. A mesh, as illustrated in Fig. 4.2, is a set of vertices, edges and faces which are connected to each other in such a way that the original geometry can be approximated by means of a polygonal one. The higher the number of elements, Fig. 4.1(a), the better the approxima-

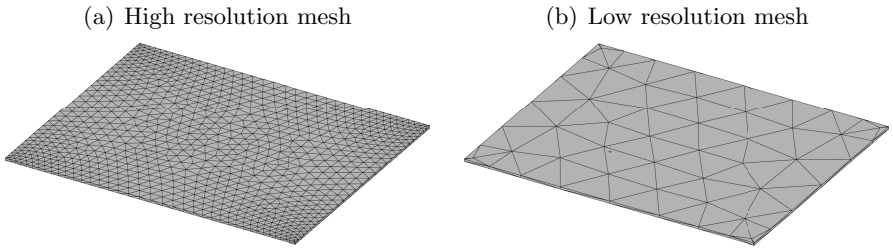

Figure 4.2: 3D CAD models of rectangular plate.

tion, on the other hand, if the number of elements is low, the model quality is poor, Fig. 4.1(b). Vertices are points that locate a position in space. Some information could be associated to each vertex , such as the vertex normal. Edges are line segments which connect two vertices. Faces are triangles, or also other simple convex polygons, defined by three (or more) vertices connected by edges. Some information could also be associated to each face, as in the case of vertices. The most important information in our case are the incenters, or centroids, and the normal vectors of the faces. Generally polygonal meshes represent only the surface of an object and the information related to the volume is implicit. In more complex cases, such as when we have used the mesh representation to solve a problem by means of FEA, we have to consider also the volumetric information and for this reason we deal with volumetric meshes. The idea behind volumetric meshes is similar to the one behind polygonal ones, in this case, however, the triangular elements are replaced by tetrahedral ones. The finite elements are therefore the faces or the volumetric elements of the mesh. The dimension (2D or 3D) is associated to each element, which defines the geometry. The value of the field or the value of its gradient, related to the geometry of the source (i.e. the displacement or the velocity), the degrees of freedom, the external forces, the mechanical properties and the boundary conditions are associated to each vertex, also called nodes, that defines the element. The FEA turns a partial differential equation into an algebraic linear system of equations as

$$\mathbf{K}\boldsymbol{\xi} = \mathbf{f}, \tag{4.1}$$

where $\mathbf{K}$ is the stiffness matrix, $\boldsymbol{\xi}$ is the displacement vector and $\mathbf{f}$ is the vector of the external forces applied to the object. The solution to the problem is given by the inversion of Eq. (4.1) that is

$$\boldsymbol{\xi} = \mathbf{K}^{-1}\mathbf{f}. \tag{4.2}$$

The stiffness matrix, as we will see in Sec. 4.2.1, includes all the information

related to the physical and mechanical parameters of the material of the object (i.e. Young's modulus, Poisson's ration, shear modulus, etc.). We have to underline that the greater the number of elements, the lower the approximation's error. As a side effect, however, using a high number of elements, the numerical complexity of the problem raises, as well as the computational time.

Now, we consider free boundary conditions and $\mathfrak{p}_1, \mathfrak{p}_2, \ldots, \mathfrak{p}_P$ combinations of the material parameters (i.e. Young's modulus, Poisson's ratio, shear modulus and density), where P is the total number of combinations. We can compute the normal velocity for each combination $\mathfrak{p}_p$ of the material parameters and for each element of the mesh. The FEA compute the normal velocity for each combination of physical parameters and for each mode of vibration identified. The FEA result is

$$\mathbf{v}_p^{\mathfrak{m}} = \begin{bmatrix} v_1(x_1, y_1, z_1) \\ v_2(x_2, y_2, z_2) \\ \vdots \\ v_N(x_N, y_N, z_N) \end{bmatrix}, \tag{4.3}$$

where $p = 1, \ldots, P$ and $\mathfrak{m} = 1, \ldots, \mathfrak{M}$ and $\mathfrak{M}$ is the total number of modes identified by FEA. N is the total number of elements of the mesh and coordinates (x_n, y_n, z_n) correspond to the centroid coordinates of the nth element. The velocity is the time derivative of the displacement in Eq. (4.2). In this way we can compute the normal velocity for each combination of the material parameters and for each mode of vibration of the source.

4.2.1 Computing the stiffness matrix

If we apply a force $\mathbf{f}$ to a spring the relation between the force applied and the deformation of the spring is defined by the Hooke's law which states that

$$\mathbf{f} = \mu \mathbf{x}, \tag{4.4}$$

where μ is a positive real number, characteristic constant of the spring and $\mathbf{x}$ is the displacement.

The strains and stresses of an elastic continuous material are related by a linear relationship similar to the Hooke's law which can be expressed as

$$\boldsymbol{\sigma} = -\boldsymbol{\kappa}\boldsymbol{\epsilon}, \tag{4.5}$$

where $\boldsymbol{\sigma}$ is the stress tensor which replace the force in the Hooke's law, $\boldsymbol{\kappa}$ is now the fourth-order tensor and is called stiffness tensor or elasticity

tensor and $\boldsymbol{\epsilon}$ is the strain tensor which can be considered equivalent to the displacement in the Eq. (4.4). In Cartesian coordinate system the strain and stress tensor can be represented in matrix form

$$\boldsymbol{\epsilon} = \begin{bmatrix} \epsilon_{xx} & \epsilon_{xy} & \epsilon_{xz} \\ \epsilon_{yx} & \epsilon_{yy} & \epsilon_{yz} \\ \epsilon_{zx} & \epsilon_{zy} & \epsilon_{zz} \end{bmatrix} \qquad \boldsymbol{\sigma} = \begin{bmatrix} \sigma_{xx} & \sigma_{xy} & \sigma_{xz} \\ \sigma_{yx} & \sigma_{yy} & \sigma_{yz} \\ \sigma_{zx} & \sigma_{zy} & \sigma_{zz} \end{bmatrix}, \tag{4.6}$$

If we consider *isotropic* materials, which their mechanical properties are independent of the direction, the Hooke's law can be rewritten in tensor notation as

$$\boldsymbol{\epsilon} = \frac{1}{E} \left(\boldsymbol{\sigma} - \nu \left[\mathrm{tr}(\boldsymbol{\sigma}) \mathbf{I} - \boldsymbol{\sigma} \right] \right), \tag{4.7}$$

where E is the Young's modulus, ν is the Poisson's ratio and with $\mathrm{tr}(\cdot)$ we denoted the *trace* of the tensor. Rewriting Eq. (4.7) in matrix form we obtain

$$\begin{bmatrix} \epsilon_{xx} \\ \epsilon_{yy} \\ \epsilon_{zz} \\ 2\epsilon_{yz} \\ 2\epsilon_{xz} \\ 2\epsilon_{xy} \end{bmatrix} = \begin{bmatrix} \epsilon_{xx} \\ \epsilon_{yy} \\ \epsilon_{zz} \\ \gamma_{yz} \\ \gamma_{xz} \\ \gamma_{xy} \end{bmatrix} = \frac{1}{E} \begin{bmatrix} 1 & -\nu & -\nu & 0 & 0 & 0 \\ -\nu & 1 & -\nu & 0 & 0 & 0 \\ -\nu & -\nu & 1 & 0 & 0 & 0 \\ 0 & 0 & 0 & 2(1+\nu) & 0 & 0 \\ 0 & 0 & 0 & 0 & 2(1+\nu) & 0 \\ 0 & 0 & 0 & 0 & 0 & 2(1+\nu) \end{bmatrix} \begin{bmatrix} \sigma_{xx} \\ \sigma_{yy} \\ \sigma_{zz} \\ \sigma_{yz} \\ \sigma_{xz} \\ \sigma_{xy} \end{bmatrix}, \tag{4.8}$$

where $\gamma_{ij} \triangleq 2\epsilon_{ij}$ is the engineering shear strain.

If we consider an *orthotropic* material, like wood, the mechanical properties are not independent from the direction. This type of material has three orthogonal planes of symmetry. Let be $(\mathbf{e}_x, \mathbf{e}_y, \mathbf{e}_z)$ the basis vector of our coordinates system. If they are normal to the planes of symmetry we can express the orthotropic stiffness matrix as

$$\begin{bmatrix} \epsilon_{xx} \\ \epsilon_{yy} \\ \epsilon_{zz} \\ 2\epsilon_{yz} \\ 2\epsilon_{xz} \\ 2\epsilon_{xy} \end{bmatrix} = \begin{bmatrix} \frac{1}{E_x} & -\frac{\nu_{xy}}{E_y} & -\frac{\nu_{xz}}{E_z} & 0 & 0 & 0 \\ -\frac{\nu_{xy}}{E_x} & \frac{1}{E_y} & -\frac{\nu_{yz}}{E_z} & 0 & 0 & 0 \\ -\frac{\nu_{xz}}{E_x} & -\frac{\nu_{yz}}{E_y} & \frac{1}{E_z} & 0 & 0 & 0 \\ 0 & 0 & 0 & \frac{1}{G_{yz}} & 0 & 0 \\ 0 & 0 & 0 & 0 & \frac{1}{G_{xz}} & 0 \\ 0 & 0 & 0 & 0 & 0 & \frac{1}{G_{xy}} \end{bmatrix} \begin{bmatrix} \sigma_{xx} \\ \sigma_{yy} \\ \sigma_{zz} \\ \sigma_{yz} \\ \sigma_{xz} \\ \sigma_{xy} \end{bmatrix}, \tag{4.9}$$

where E_i is the Young's modulus along i axis, G_{ij} is the shear modulus in j direction on the plane whose normal is in direction i and ν_{ij} is the Poisson's ration which corresponds to a contraction in direction j when an extension is applied in direction i.

4.3 Equivalent sources

Looking at Eq. (2.29) we can observe that the modes' shape, from a theoretical point of view and under ideal conditions, is invariant with respect to the physical parameters of the material, and it is related only to the geometrical properties. On the ground of this we can suppose that in real situations the modes' shape of more complex geometry slightly varies with respect to the physical parameters of the material. Our hypothesis is confirmed from simulation results obtained analysing a complex geometry for a large set of material parameters by means of FEA, as discussed in Sec. 4.2. Moreover, back-propagating the normal velocity to the equivalent sources, we observed that the equivalent source weights, for different physical parameters combinations, are highly correlated. Therefore, by means of a linear combination of the equivalent source weights, we can retrieve the surface velocity for all possible value of the physical parameters. In other words, equivalent source weights can be interpreted as basis functions which allow us to compute the surface velocity.

4.3.1 Computing the equivalent source weights

Starting from the normal velocity, computed for each element of the mesh by means of FEA, and inverting Eq. (3.56), we can compute the equivalent source weights. The procedure to compute the equivalent source weights $\mathbf{q}_p^{\mathfrak{m}}$ must be repeated for every $p = 1, \ldots, P$ parameters combinations and for all the $\mathfrak{m} = 1, \ldots, \mathfrak{M}$ modes of vibration of the source identified by the FEA in the frequency range analysed as seen in Sec. 4.2. The matrix $\mathbf{G}_{sv}$ defined in Eq. (3.58) is the Green's function matrix that relates the equivalent sources and the points of the source (incenters of the mesh). The equivalent source weigths, for each combination $\mathfrak{p}$ are defined as

$$\mathbf{q}_p^{\mathfrak{m}} = \mathbf{G}_{sv}^{\dagger} \mathbf{v}_p^{\mathfrak{m}}, \tag{4.10}$$

where $p = 1, \ldots, P$, $\mathbf{v}_p^{\mathfrak{m}} \in \mathbb{R}^{N \times 1}$ is the velocity vector of the source computed by means of FEA, $\mathbf{q}_p^{\mathfrak{m}} \in \mathbb{C}^{U \times 1}$ and $\mathbf{G}_{sv}^{\dagger}$ is the pseudo-inverse of the matrix $\mathbf{G}_{sv} \in \mathbb{C}^{N \times U}$ computed by means of the SVD, N is the number of elements of the mesh and U is the number of equivalent sources. Since the problem is

ill-conditioned the inversion of the matrix $\mathbf{G}_{sv}$ cannot be performed directly, but we have to use a regularization technique. As in the case presented in Sec. 3.4, we use the Tikhonov regularization [10] combined with the L-curve method [12] to choose the regularization parameter λ. The problem can be reformulated as

$$\arg\min_{\mathbf{q}_p^{\mathfrak{m}}} \|\mathbf{G}_{sv}\mathbf{q}_p^{\mathfrak{m}} - \mathbf{v}_p^{\mathfrak{m}}\|_2^2 + \lambda^2 \|\mathbf{I}\mathbf{q}_p^{\mathfrak{m}}\|_2^2. \tag{4.11}$$

The L-curve method plots the term $\|\mathbf{\Gamma}\mathbf{q}_p^{\mathfrak{m}}(\lambda)\|$ versus the term $\|\mathbf{G}_{sv}\mathbf{q}_p^{\mathfrak{m}} - \mathbf{v}_p^{\mathfrak{m}}\|$ in a graph, where $\mathbf{q}_p^{\mathfrak{m}}(\lambda)$ is the solution to Eq. (4.11) in function of the regularization parameter λ and $\mathbf{\Gamma} = \lambda\mathbf{I}$ is the Tikhonov matrix. In a more elegant way we can define the L-curve as a continuous curve constituted by the points $\left(\|\mathbf{G}_{sv}\mathbf{q}_p^{\mathfrak{m}}(\lambda) - \mathbf{v}_p^{\mathfrak{m}}\|, \|\mathbf{\Gamma}\mathbf{q}_p^{\mathfrak{m}}(\lambda)\|\right)$, for $\lambda \in [0, \infty)$. If we plot these points, varying λ, on a *log-log* plot we obtain a curve whose shape is similar to an "L". The optimal λ value is the one that corresponds to the solution $\mathbf{q}_p^{\mathfrak{m}}(\lambda)$ near the "corner" which guarantees a good compromise between a small residual norm $\|\mathbf{G}_{sv}\mathbf{q}_p^{\mathfrak{m}}(\lambda) - \mathbf{v}_p^{\mathfrak{m}}\|$ and a small solution seminorm $\|\mathbf{\Gamma}\mathbf{q}_p^{\mathfrak{m}}(\lambda)\|$.

4.3.2 Equivalent sources positioning

The positioning of the equivalent sources is not a trivial aspect since the performances of the ESM are related to this. In literature there are few studies [14] about this argument. The correct positioning of the equivalent sources is affected by many parameters in particular the distance from the source surface and the spacing of the grid. The equivalent sources and the microphones are positioned on a 2D grid. Fig. 4.3 depicts a cross-section view of the hologram plane, the source surface and the equivalent sources plane. The distance between the microphones and the sources is $\mathrm{d_h}$ and the distance between the source surface and the equivalent sources plane is $\mathrm{d_q}$. The lattice spacing of the microphones grid is $\Delta\mathrm{x_h}$ and $\Delta\mathrm{y_h}$ in x and y directions respectively. The equivalent sources spacing is $\Delta\mathrm{x_q}$ and $\Delta\mathrm{y_q}$ in directions x and y respectively.

Since it does not exist a relation that gives us the optimal distance and the optimal grid spacing, we have conducted preliminary simulation to determine the best positioning of the equivalent sources. The simulation results have highlighted that the equivalent sources have to be placed approximatively specular with respect to the measurement plane to obtain better results. Moreover, as explained in Sec. 3.4, the spacing of the equivalent sources lattice has to be slightly smaller than the measurement spacing. In particular we notice that the distance $d_h \approx d_q$. The lattice spacing $\Delta x_q, y_q$,

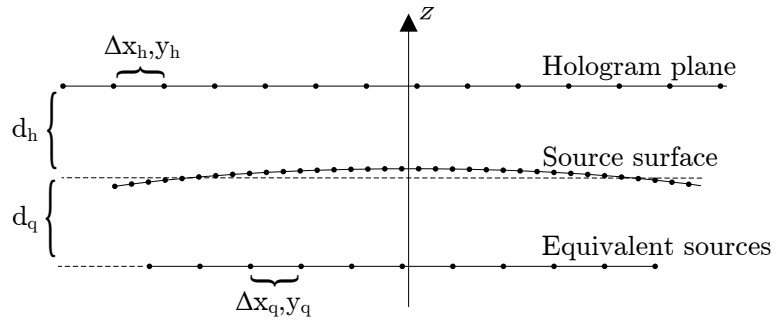

Figure 4.3: Hologram plane and equivalent sources plane positions with respect to the source surface and related lattice spacing.

of the equivalent sources in x and y directions, has to be smaller than the grid spacing of the measurement points $\Delta x_h, y_h$, as explained in Sec. 3.4.

4.4 Dictionary design

The information in the dataset of equivalent source weights are computed for each combination of physical parameters and for each mode. By means of the Principal Component Analysis (PCA), we can design the dictionary of equivalent source weights which will be used combined to the ESM to solve the NAH problem.

4.4.1 Dataset preprocessing

First to proceed we have to reorganize the dataset. For each mode $\mathfrak{m}$ identified by the FEA we have to group all the equivalent source weights computed for each combination of parameters. We define the matrix $\mathbf{Q}^{\mathfrak{m}}$ as

$$\mathbf{Q}^{\mathfrak{m}} = \left[\mathbf{q}_1^{\mathfrak{m}}, \mathbf{q}_2^{\mathfrak{m}}, \ldots, \mathbf{q}_p^{\mathfrak{m}}, \ldots, \mathbf{q}_P^{\mathfrak{m}}\right], \tag{4.12}$$

where the matrix $\mathbf{Q}^{\mathfrak{m}}$ has size $U \times P$ and $\mathfrak{m} = 1, \ldots, \mathfrak{M}$. Now we have $\mathfrak{M}$ matrices, one for each mode of vibration of the source, whose columns correspond to the equivalent source weights computed for each combination of parameters.

Since we observed that the modes shape slightly change respect to the variation of the physical parameters and this is true also for the equivalent source weights, the column vectors of the matrix $\mathbf{Q}^{\mathfrak{m}}$, in Eq. (4.12), are highly correlated, therefore we can compress the amount of data and reduce the size of the dataset. This operation can be done by means of the PCA [17].

4.4.2 Principal component analysis

The PCA aims at extracting the most important information from the data and reducing the size of the dataset, keeping only the relevant part of the information. In order to do this the PCA computes new variables, which are a linear combination of the original ones, called principal components. Mathematically we can define the PCA as a set of p-dimensional vectors of coefficients $\mathbf{w}_a$, called *loads*, which map every row vector $\mathbf{q}_b$ (p and $\mathfrak{m}$ are omitted for clarity reasons) of $\mathbf{Q}^{\mathfrak{m}}$ to a new vector of principal component $\mathbf{s}_b = (s_1, \ldots, s_a)_b$, called *scores*, given by $s_{ab} = \mathbf{q}_b \cdot \mathbf{w}_a$. The first component is computed in such a way that it has the largest possible variance, thus the first loading vector has to satisfy

$$\mathbf{w}_1 = \underset{\|\mathbf{w}\|=1}{\arg\max} \left(\sum_b (s_1)_b^2 \right) = \underset{\|\mathbf{w}\|=1}{\arg\max} \left(\sum_b (\mathbf{q}_b \cdot \mathbf{w})^2 \right) \tag{4.13}$$

or in matrix form

$$\mathbf{w}_1 = \underset{\|\mathbf{w}\|=1}{\arg\max} \left(\|\mathbf{Q}^{\mathfrak{m}}\mathbf{w}\|^2 \right) = \underset{\|\mathbf{w}\|=1}{\arg\max} \left(\mathbf{w}^T \left(\mathbf{Q}^{\mathfrak{m}}\right)^T \mathbf{Q}^{\mathfrak{m}}\mathbf{w} \right) \tag{4.14}$$

The ath component ($a \geq 2$) must be orthogonal to the previous $a-1$ principal components of $\mathbf{Q}^{\mathfrak{m}}$ and must have the largest possible variance. The ath component can be computed subtracting the first $a-1$ component from $\mathbf{Q}^{\mathfrak{m}}$

$$\hat{\mathbf{Q}}_a^{\mathfrak{m}} = \mathbf{Q}^{\mathfrak{m}} - \sum_{l=1}^{a-1} \mathbf{Q}^{\mathfrak{m}}\mathbf{w}_l\mathbf{w}_l^T, \tag{4.15}$$

and finding the loading vector

$$\mathbf{w}_a = \underset{\|\mathbf{w}\|=1}{\arg\max} \left(\|\hat{\mathbf{Q}}_a^{\mathfrak{m}}\mathbf{w}\|^2 \right) = \arg\max \left(\frac{\mathbf{w}^T \left(\hat{\mathbf{Q}}_a^{\mathfrak{m}}\right)^T \hat{\mathbf{Q}}_a^{\mathfrak{m}}\mathbf{w}}{\mathbf{w}^T\mathbf{w}} \right) \tag{4.16}$$

The full PCA of the matrix $\mathbf{Q}^{\mathfrak{m}}$ can be expressed in matrix form as

$$\mathbf{S}^{\mathfrak{m}} = \mathbf{Q}^{\mathfrak{m}}\mathbf{W}, \tag{4.17}$$

where $\mathbf{W}$ is a $P \times P$ matrix whose columns are the eigenvectors of $\left(\mathbf{Q}^{\mathfrak{m}}\right)^T \mathbf{Q}^{\mathfrak{m}}$.

The PCA can be associated to the SVD. If

$$\mathbf{Q}^{\mathfrak{m}} = \mathbf{U}\mathbf{\Sigma}\mathbf{W}^T \tag{4.18}$$

is the SVD of the matrix $\mathbf{Q}^{\mathfrak{m}}$ we can write the score matrix $\mathbf{S}^{\mathfrak{m}}$ as

$$\mathbf{S}^{\mathfrak{m}} = \mathbf{Q}^{\mathfrak{m}}\mathbf{W} = \mathbf{U}\mathbf{\Sigma}\mathbf{W}^T\mathbf{W} = \mathbf{U}\mathbf{\Sigma}. \tag{4.19}$$

To reduce the dimension of the dataset we have to compute the cumulative energy content for each eigenvector of the empirical covariance matrix that is proportional to the matrix $(\mathbf{Q}^{\mathfrak{m}})^T \mathbf{Q}^{\mathfrak{m}}$. The matrix $\mathbf{W}$ diagonalizes this matrix and we can obtain the diagonal matrix $\mathbf{\Lambda}$ whose elements are the eigenvalues of $(\mathbf{Q}^{\mathfrak{m}})^T \mathbf{Q}^{\mathfrak{m}}$ as

$$\mathbf{W}^{-1} \left((\mathbf{Q}^{\mathfrak{m}})^T \mathbf{Q}^{\mathfrak{m}} \right) \mathbf{W} = \mathbf{\Lambda}. \tag{4.20}$$

Sorting the eigenvectors $\mathbf{W}$ and the eigenvalues $\mathbf{\Lambda}$ matrices in order to decrease eigenvalues and maintain the correct pairings between the columns of each matrix, we can compute the cumulative energy for each eigenvector. The cumulative energy for the ath eigenvector is

$$\mathcal{E}(a) = \sum_{b=1}^{a} [\mathbf{\Lambda}]_{b,b} \qquad \text{for} \qquad a = 1, \ldots, P. \tag{4.21}$$

We have to keep only the first $\mathcal{L}$ components according to

$$\frac{\mathcal{E}(\mathcal{L})}{\mathcal{E}(P)} \geq t_h, \tag{4.22}$$

where t_h is a fixed threshold. The transformation becomes

$$\mathbf{S}_{\mathcal{L}}^{\mathfrak{m}} = \mathbf{U}_{\mathcal{L}} \mathbf{\Sigma}_{\mathcal{L}} = \mathbf{Q}^{\mathfrak{m}} \mathbf{W}_{\mathcal{L}}. \tag{4.23}$$

Performing the PCA of the matrix $\mathbf{Q}^{\mathfrak{m}}$ for each mode we obtain $\mathfrak{M}$ matrices $\mathbf{S}_{\mathcal{L}}^{\mathfrak{m}} \in \mathbb{C}^{U \times \mathcal{L}}$. The set $\mathcal{D}$ of these matrices is the dictionary and can be represented in matrix form concatenating the $\mathfrak{M}$ matrices as

$$\mathbf{D} = \left[\mathbf{S}_{\mathcal{L}}^{1}, \mathbf{S}_{\mathcal{L}}^{2}, \ldots, \mathbf{S}_{\mathcal{L}}^{\mathfrak{M}} \right]. \tag{4.24}$$

The dictionary obtained in Eq. (4.24) includes the principal components, whose contribution is greater than or equal to the threshold t_h in Eq. (4.22), of the equivalent source weights computed from the normal velocity of each mode identified by the FEA.

4.5 The NAH problem

In Sec. 4.3 we have seen how the equivalent sources are positioned and how we can compute their weights starting from the normal velocity of the source computed numerically by means of FEA. In Sec. 4.4 we have discussed the design of the dictionary using the PCA.

By means of Eq. (3.52) we can compute the pressure on the hologram plane given the equivalent source weights. If we consider the dictionary we can rewrite this equation as

$$\mathbf{p}_h = j\rho_0 ck \mathbf{G}_{hp}\mathbf{q} = j\rho_0 ck \mathbf{G}_{hp}\mathbf{D}\boldsymbol{\gamma}, \tag{4.25}$$

where $\boldsymbol{\gamma}$ is the *driving vector* of the dictionary. The vector $\boldsymbol{\gamma}$, if we had properly designed the dictionary, has only a few elements different from zero since we are in a sparse domain. As in Sec. 3.4, we have to invert Eq. (4.25) to find the driving vector of the dictionary according to the pressure measured on the hologram plane as

$$\boldsymbol{\gamma} = \frac{1}{j\rho_0 ck} \left(\mathbf{G}_{hp}\mathbf{D}\right)^{\dagger} \mathbf{p}_h. \tag{4.26}$$

The Least-Squares solution does not guarantee that the vector $\boldsymbol{\gamma}$ is sparse. Therefore we have to use another technique called Least Absolute Shrinkage and Selection Operator (LASSO) regression [18] which promotes sparsity. The LASSO regression shrinks some coefficients and moreover sets the others to zero, choosing, in that way, a simpler model that does not include those coefficients. Rewriting Eq. (4.26) using the LASSO regression we obtain

$$\arg\min_{\boldsymbol{\gamma}} \left(\frac{1}{M} \|\mathbf{p}_h - \mathbf{G}_{hp}\mathbf{D}\boldsymbol{\gamma}\|_2^2 \right) \qquad \text{subject to} \qquad \|\boldsymbol{\gamma}\|_1 \leq \mathcal{T}, \tag{4.27}$$

where M is the number of measurements, and $\mathcal{T}$ is a parameter which determines the amount of regularization. We can also express Eq. (4.27) in the Lagrangian form as

$$\arg\min_{\boldsymbol{\gamma}} \left(\frac{1}{M} \|\mathbf{p}_h - \mathbf{G}_{hp}\mathbf{D}\boldsymbol{\gamma}\|_2^2 + \lambda \|\boldsymbol{\gamma}\|_1 \right), \tag{4.28}$$

where λ is the regularization parameter. The optimal regularization parameter λ_{opt} has to be chosen using the Generalized Cross-Validation method [19].

At this point, we can reconstruct the source velocity as

$$\mathbf{v} = \mathbf{G}_{sv}\mathbf{q} = \mathbf{G}_{sv}\mathbf{D}\boldsymbol{\gamma}. \tag{4.29}$$

The driving vector $\boldsymbol{\gamma}$ selects only a few column vectors of the dictionary, more precisely it selects only those that correspond to the equivalent sources which best describe the pressure measured on the hologram plane.

Performing some simulation we noticed that this is true only if the number of column vectors in the matrix $\mathbf{D}$ is limited, that is, only if a few modes are represented by the dictionary entries. To enhance the performance of the dictionary we have to search for a subset of the full dictionary and then use this subset to solve the problem in Eq. (4.28).

4.5.1 Optimal dictionary subset search

To find the optimal subset we have to find those modes of vibration of the source, or equivalently their corresponding equivalent sources, which best describe the pressure measured on the hologram. To do so we have to define a cost-function. Let $\mathbf{s}_1^{\mathfrak{m}}$ be the first column vector of the matrix $\mathbf{S}_{\mathcal{L}}^{\mathfrak{m}}$ in Eq. (4.23). We can approximate the hologram pressure considering only the first principal component $\mathbf{s}_1^{\mathfrak{m}}$, for $\mathfrak{m} = 1, \ldots, \mathfrak{M}$ by

$$\tilde{\mathbf{p}}_h^{\mathfrak{m}}(\varphi) = j\rho_0 ck \mathbf{G}_{hp}\, \mathbf{s}_1^{\mathfrak{m}}\, e^{j\varphi}, \tag{4.30}$$

where $e^{j\varphi}$ is an unknown phase term. Since the modulus is unknown as well, we have to normalize the vectors $\tilde{\mathbf{p}}_h^{\mathfrak{m}}(\varphi)$ and $\mathbf{p}_h$. Now it is possible to compute the cost-function as

$$\mathcal{R}(\mathfrak{m}, \varphi) = \| \frac{\mathbf{p}_h}{\|\mathbf{p}_h\|} - \frac{\tilde{\mathbf{p}}_h^{\mathfrak{m}}(\varphi)}{\|\tilde{\mathbf{p}}_h^{\mathfrak{m}}(\varphi)\|} \|. \tag{4.31}$$

Minimizing the cost-function in Eq. (4.31) with respect to $(\mathfrak{m}, \varphi)$ we can obtain the mode index $\hat{\mathfrak{m}}$ we are looking for as

$$\arg\min_{(\mathfrak{m},\varphi)} \mathcal{R}(\mathfrak{m}, \varphi) = \arg\min_{(\mathfrak{m},\varphi)} \| \frac{\mathbf{p}_h}{\|\mathbf{p}_h\|} - \frac{\tilde{\mathbf{p}}_h^{\mathfrak{m}}(\varphi)}{\|\tilde{\mathbf{p}}_h^{\mathfrak{m}}(\varphi)\|} \|. \tag{4.32}$$

Knowing the mode index $\hat{\mathfrak{m}}$ it is now possible to select the subset $\mathcal{D}_{\hat{\mathfrak{m}}} \subset \mathcal{D}$ and defining the corresponding matrix $\mathbf{D}_{\hat{\mathfrak{m}}}$ as

$$\mathbf{D}_{\hat{\mathfrak{m}}} = \left[\mathbf{S}_{\mathcal{L}}^{\hat{\mathfrak{m}}} \right]. \tag{4.33}$$

Since the pressure $\tilde{\mathbf{p}}_h^{\mathfrak{m}}(\varphi)$ is only an approximation and the measured pressure can be corrupted by noise, the minimization process, in Eq. (4.32), could retrieve an erroneous mode index. To overcome this problem, it is possible to consider a larger subset $\mathcal{D}_{(\hat{\mathfrak{m}}|\mathcal{M})}$ which does not only include the information of the mode index $\hat{\mathfrak{m}}$, but also the information of the modes around it $(\hat{\mathfrak{m}}|\mathcal{M}) = (\hat{\mathfrak{m}} - \mathcal{M}, \hat{\mathfrak{m}} + \mathcal{M})$. $\mathcal{M}$ is an integer number that identifies how many additional modes we want to add. We fix $\mathcal{M} = 1$, in this way we consider a dictionary subset containing the information related to three modes. Using this configuration we can deal with inter-modal behaviour of the source and moreover tolerate a little error in the mode identification process. If we add a greater number of additional modes the performances get worse.

The dictionary matrix can be rewritten as

$$\mathbf{D}_{(\hat{\mathfrak{m}}|\mathcal{M})} = \left[\mathbf{S}_{\mathcal{L}}^{\hat{\mathfrak{m}}-\mathcal{M}}, \ldots, \mathbf{S}_{\mathcal{L}}^{\hat{\mathfrak{m}}}, \ldots, \mathbf{S}_{\mathcal{L}}^{\hat{\mathfrak{m}}+\mathcal{M}} \right], \tag{4.34}$$

and the Eqs. (4.28) and (4.29) can be recast as

$$\arg\min_{\boldsymbol{\gamma}} \left(\frac{1}{M} \|\mathbf{p}_h - \mathbf{G}_{hp}\mathbf{D}_{(\hat{\mathfrak{m}}|\mathcal{M})}\boldsymbol{\gamma}\|_2^2 + \lambda\|\boldsymbol{\gamma}\|_1 \right), \tag{4.35}$$

and

$$\mathbf{v} = \mathbf{G}_{sv}\mathbf{q} = \mathbf{G}_{sv}\mathbf{D}_{(\hat{\mathfrak{m}}|\mathcal{M})}\boldsymbol{\gamma}. \tag{4.36}$$

allowing us to reconstruct the normal velocity of the source starting from the pressure measurement.

Remarks

The use of the dictionary allows us to improve the robustness of the ESM. The equivalent source's weights are not computed directly from the pressure measurements as in the ESM case, but are precomputed by FEA of the source geometries considering a large set of different physical parameters and taking the principal components. Then, we only have to select them from the dictionary according to the pressure measured on the hologram plane.

In the next chapter we will illustrate how it is possible to implement the proposed method in MATLAB® in particular focusing our attention on the CAD model and MATLAB® toolboxes. In Chapter 6 we will present our simulation and experimental results.

Chapter 5

System realization

In this chapter we describe the tools employed for implementing the proposed methodology. The whole framework has been realized in MATLAB®, and we exploited some built-in and third-party toolboxes for accomplishing some specific tasks. More specifically, we have to analyse some aspects related to CAD model, how to import a mesh file in MATLAB®, and how the Partial Differential Equation Toolbox™ (PDE toolbox) works. In particular, we focus our attention to the definition of the stiffness matrix for *orthotropic* materials, such as wood. Finally we will illustrate the third-party toolboxes to implement the Tikhonov regularization combined with the L-curve method and the LASSO regression.

5.1 Finite element analysis

In this section we describe how we implemented the FEA. In particular we will illustrate the STL mesh format used to import the CAD model file in MATLAB® and the built-in PDE toolbox™ which we had used to compute the normal velocity of the source as explained in Sec.4.2.

5.1.1 STL mesh format

As explained in Sec. 4.2 to perform the FEA the geometry of the source has to be discretized. This operation can be done using a mesh. The CAD model is composed by a finite number of element of predefined shape. The mesh geometry is an approximation of the original geometry of the source: the greater the number of elements composing the mesh, the better the approximation. The mesh is a set of vertices, edges and faces. The vertices are points in space that identify a position, generally they correspond to points on the object surface. Edges are line segments which connect two

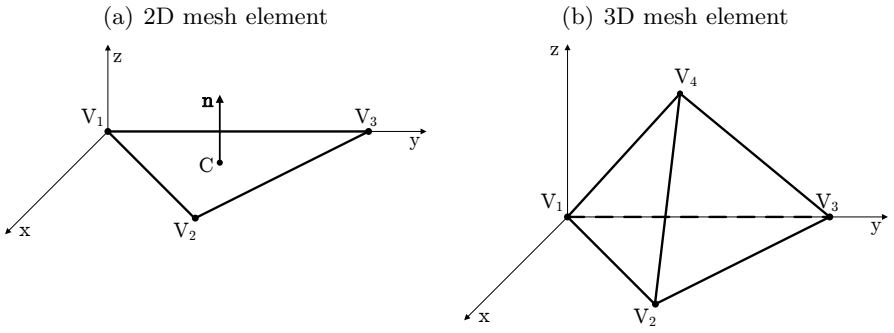

Figure 5.1: Polygonal and volumetric mesh linear elements.

vertices. Faces are usually triangles (or other simple convex polygons) constituted by three connected vertices. This kind of mesh is called polygonal mesh with *linear* elements. In more complex cases, as seen in Sec. 4.2, the volume information cannot be implicit, therefore we have to consider a complex model, a volumetric mesh. The idea is the same, in this case the faces are not 2D linear elements, but are 3D linear elements and the triangular faces are replaced with tetrahedral elements. Also in this case edges connect two vertices and vertices identify a position in space. Fig. 5.1(a) depicts a 2D linear element of a mesh. For each element of the mesh we can define the centroid, C, or incenter, of the face and also its the normal vector, $\mathbf{n}$. This information is very useful to deal with the orientation of an element respect the direction of a field (e.g. velocity field). Fig. 5.1(b) illustrates a 3D linear element of a volumetric mesh. To improve the quality of the model it is possible to use *quadratic* elements, rather than the linear ones. Quadratic elements have six points per element in 2D cases and ten points per element in 3D cases. In addition to the vertices, the quadratic elements use the midpoint of each edge.

The simplest representation of a mesh with linear elements is done using two matrices. The first matrix contains the information related to the spatial position of the vertices (i.e cartesian coordinates (x, y, z)). This matrix has dimensions $N_V \times 3$, where the number of rows is the number of vertices and the columns are relative to the three spatial coordinates. The total number of rows represents the number of vertices in the mesh. The second matrix is the connectivity list, with dimensions $N_E \times N_C$. Each row corresponds to a mesh element and in the columns are inserted the vertices indices that compose the element. The number of a row corresponds to the face index. If we are dealing with volumetric mesh the connectivity list has four columns instead of three. With reference to Fig. 5.1(a), Tab. 5.1 depicts the Vertices

Vertex index	x-coordinate	y-coordinate	z-coordinate
V_1	0.0	0.0	0.0
V_2	2.0	1.5	0.0
V_3	0.0	3.0	0.0

Table 5.1: Vertices coordinates of the mesh element in Fig. 5.1(a).

Face index	1^{st} vertex index	2^{nd} vertex index	3^{rd} vertex index
F_1	V_1	V_2	V_3

Table 5.2: Connectivity list of the mesh element in Fig. 5.1(a).

coordinates and Tab. 5.2 reports the related connectivity list. This representation of the mesh is used in STereo Lithography interface format (STL) file. This type of file is used to import mesh models in MATLAB® to use it in the PDE toolbox™.

5.1.2 Partial Differential Equation toolbox™

The Partial Differential Equation toolbox™ (PDE toolbox™) is a MATLAB® toolbox to solve numerically partial differential equations. We use this toolbox to perform the FEA. To perform the FEA we have to import the object CAD model, set the boundary conditions, set the analysis frequency range, define the stiffness matrix and choose the appropriate solver in the PDE toolbox™.

Importing the CAD model

To import a STL file in MATLAB® we have to use the commands

```
file = ['ViolinTopPlate3D.stl']; % CAD model file
model = createpde(3);
importGeometry(model,file);
```

The command `createpde()` is used to create the `model` variable. This variable includes four fields:

```
model.PDESystemSize
model.Geometry
model.BoundaryConditions
model.Mesh
```

The PDE system size is fixed by the user and corresponds to the argument of the function `createpde()`, in our case it is set to three since we are working

in a 3D space. By means of the function `importGeometry()`, we import the CAD model into MATLAB® and the information related to the number of faces, edges and vertices are included in the model.Geometry field.

The next step is to create the volumetric mesh starting from the polygonal one. To do so, we use the command

```
generateMesh(model,'Hmax',hmax,'Hmin',hmin,...
        'GeometricOrder','quadratic');
```

This function allows us to set the maximum and minimum length of the edges of the elements and we can therefore set the precision of the approximation. Moreover we can choose to use linear or quadratic elements. It is important to notice that the shorter the length of the edges, the higher the number of elements, and therefore the better the quality of the mesh model. The drawback is due to the fact that using an high number of elements raises the numerical complexity, as well as the computational time. The result of this function is inserted in the model.Mesh field. Here we can find the *Nodes* and the *Elements* matrices with a structure similar to the one illustrated before in Tabs. 5.1 and 5.2.

Setting the boundary conditions

To set the boundary conditions we can use the command

```
applyBoundaryCondition(model,'face',1:4,'u',0);
```

Here we can specify with the second argument, `(RegionType, RegionID)`, to which faces the boundary conditions are applied. The third parameter, `(Name, Value)`, of the function allows us to select which type of boundary conditions we want to use (i.e. Dirichlet or Neumann boundary condition) and their value. The result is inserted in the respective field of the `model` data structure. In the example we apply the Dirichlet boundary conditions equal to zero, to the faces from one to four of the mesh.

In our simulation since we want to analyse the free motion of the source this function is not utilised.

Selecting the solver

Now, to find the modes of vibration of the object we have to choose the appropriate solver of the PDE toolbox™. To find the modes of vibration and the associated eigen frequencies we have to solve a eigenvalue-eigenvector problem, therefore we select the `pdeeig()` solver. The MATLAB® code is the following

```
[eVec,eVal] = pdeeig(model,c,a,rho,r);
```

and the equation implemented by this function is

$$-\nabla \cdot (\mathbf{c} \otimes \nabla \xi) + \mathbf{a}\,\xi = \tau \rho\, \xi, \tag{5.1}$$

where ξ corresponds to the displacement of the object ad τ is the eigenvalue of the problem corresponding to the eigen-frequency. The `c` parameter corresponds to the *stiffness* matrix seen in Sec. 4.2.1. This parameter, for an *isotropic* material, such as aluminium, can be computed by the MATLAB® command

```
c = elasticityC3D(E,nu)
```

The variable `E` represents the Young's modulus and `nu` is the Poisson's ratio. For an *orthotropic* material, such as wood, we have to implement a function to convert the matrix in Eq. (4.9) in the toolbox form as

```
c = orthotropicStiffnessMatrix(Ex,Ey,Ez,nu_xy,nu_xz,nu_yz,Gxy,
    Gxz,Gyz);
```

as explained in the PDE toolbox™ user guide. The variables `Ex`, `Ey`, `Ez` correspond to the Young's modulus for the x, y and z coordinates, the variables `nu_xy, nu_xz, nu_yz` correspond to the Poisson's ratio and `Gxy, Gxz, Gyz` to the shear modulus.

The `a` parameter of the `pdeeig()` solver, in our case, is the displacement of the object and have to be set to zero since is not part of the Kirchhoff-Love equation which describes the object motion. The `rho` parameter is the density of the material of the object and `r` is the analysis frequency range defined as $\omega^2_{\min} \leq \omega^2 \leq \omega^2_{\max}$, where $\omega = 2\pi f$ and f is the frequency. The output `eVec` of the `pdeeig()` function corresponds to the eigenvector which describes the mode shape of the object and the variable `eVal` is the eigenvalue τ associated to the eigen-frequency of the mode. The eigen-frequency can be computed as $f_{\text{eig}} = \frac{\sqrt{\tau}}{2\pi}$.

Now, by means of the PDE toolbox™ we can compute the modes shape of any object starting from its CAD model and its mechanical and physical material parameters.

Computing the normal velocity

Since we are interested in the normal displacement or normal velocity of the surface of the object, we have to extract this information from the PDE toolbox ™ result using the following code

```
% PDE result
result = createPDEResults(model,eVec);
rs = result.NodalSolution;
[p,~,t] = model.Mesh.meshToPet();
argin = {'flowdata',rs(:,:,mode)};

parser = inputParser;
addParameter(parser,'flowdata', [], @isnumeric);
parse(parser,argin{:});
flowdata = parser.Results.flowdata;
```

With the function `result = createPDEResults()`, we create the `result` data structure. In this variable we find the solution related to each node of the mesh. Using the `parse` command we can compute the `flowdata` variable, that is we have the displacement for each node of the mesh with respect to its resting position. Since we want only the data on the surface of the object we have to retrieve the surface points of the volumetric mesh. To do this operation we redefine the triangulation of the volumetric mesh, then we select only those points that are on the surface by means of the function `freeBoundary(text)`. The MATLAB® code is the following

```
%3D geometry
nodesT4 = unique(t(1:4,:));
dt = triangulation(t(1:4,:)', p(:,nodesT4)');

% Surface
[T,Xb] = freeBoundary(dt);
TR = triangulation(T,Xb);
```

At this point we have a polygonal mesh which represents only the surface of the object. By means of the following function we can compute the incenter and the normal of each face. Moreover we can compute the vertex normal, the vertex coordinates, also called nodes, and the connectivity list as

```
% Calculate incenters, face and vertex normals.
inctr = incenter(TR);
fn = faceNormal(TR);
vn = vertexNormal(TR);

% Polygonal mesh
nodes = TR.Points;
elements = TR.ConnectivityList;
```

Now it is possible to compute the displacement of the surface of the object. To do so we have to interpolate the results by means of the function `pdeInterpolant()` and then evaluate the results in correspondence of the

incenters or the nodes. Finally computing the *dot product* between the displacement and the normal we find the normal displacement as

```
% Create the interpolant
F = pdeInterpolant(p,t,flowdata);

% Interpolate results
FEMoutINCENTER = evaluate(F,inctr(:,1),inctr(:,2),inctr(:,3));
FEMoutVERTEX = evaluate(F,nodes(:,1),nodes(:,2),nodes(:,3));

% Projection - normal displacement component
normDisp(:,mode) = dot(FEMoutINCENTER,fn,2);
normDispVertex(:,mode) = dot(FEMoutVERTEX,vn,2);
```

At this point we have all the necessary information to implement the Dictionary-based ESM proposed in Chapter 4. Starting from the normal displacement we can derive the normal velocity as

$$\mathbf{v} = j\omega\boldsymbol{\xi}_{\mathrm{FEA}}, \tag{5.2}$$

where j is the imaginary unit, ω is the angular frequency and $\boldsymbol{\xi}_{\mathrm{FEA}}$ is the displacement vector computed by means of FEA. Fig. 5.2 depicts the first four free modes of vibration of a rectangular top plate computed by means of FEA.

5.2 Near-field Acoustic Holography

To implement the Dictionary based ESM we use other toolboxes in addition to the PDE toolbox™.

5.2.1 Computing the equivalent source weights

To compute the equivalent source weights, as described in Sec. 4.3, we have to use a regularization technique since the problem in Eq. (4.10) is ill-conditioned. The regularization technique that we have used is the Tikhonov regularization [10] combined with the L-curve method [12] to choose the regularization parameter λ. To implement the Tikhonov regularization and the L-curve method in MATLAB® we can use these functions

```
%Compact SVD
[U,s,V] = csvd(Gsv);

%L-curve
[lambda,~,~,~] = l_curve(U,s,us,'Tikh','off');
%Tikhonov regularization
[q(:,obs),~,~] = tikhonov(U,s,V,us,lambda);
```

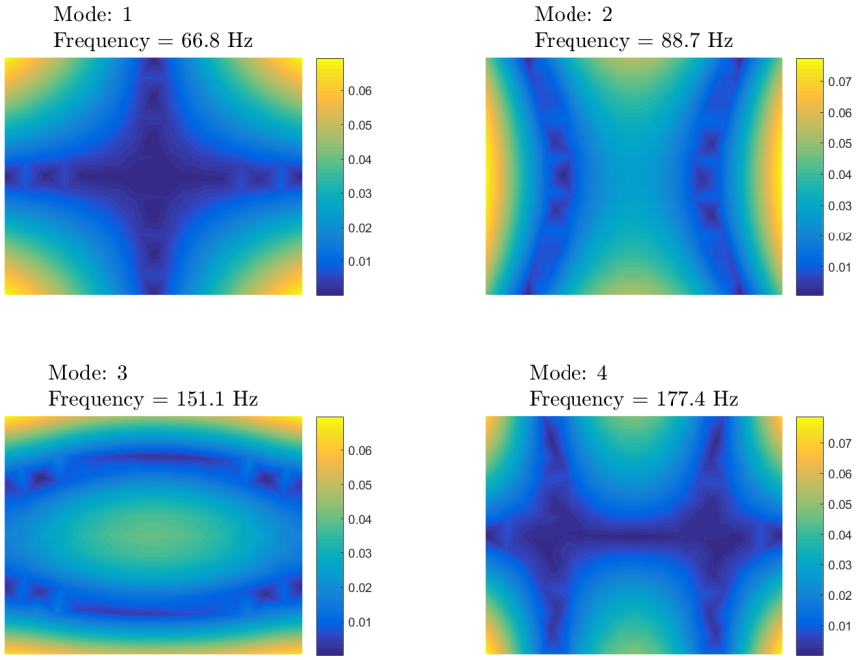

Figure 5.2: FEA results of the first four mode of the free rectangular plate. In figure is shown the absolute value to highlight the nodal lines (top view).

which are included in the *regtools* toolbox - Copyright © 2015, Per Christian Hansen [20]. The variable `Gsv` represents the matrix $\mathbf{G}_{sv}$ in Eq. (4.10) which has to be inverted. In Fig. 5.3 is depicted the L-curve used to find the λ parameter.

5.2.2 Principal component analysis

To compute the PCA, as illustrated in Sec.4.4.2, there exists a specific MATLAB® function

```
%PCA Algorithm: svd(default),eig,als
[coeff,score,~,~,explained,mu] = pca(data,'Algorithm','svd','
    Centered',false);
```

This function receives as input the dataset, represented by the variable `data`, the type of the algorithm used to perform the PCA, while the flag `centered` enables data centering with respect to the mean, if set to true. The function returns the coefficient and score matrices, the mean value vector of the dataset, `mu`, and the principal component relevance vector, `explained`. The information in the variable `explained` is used to define the number of principal component we have to keep as

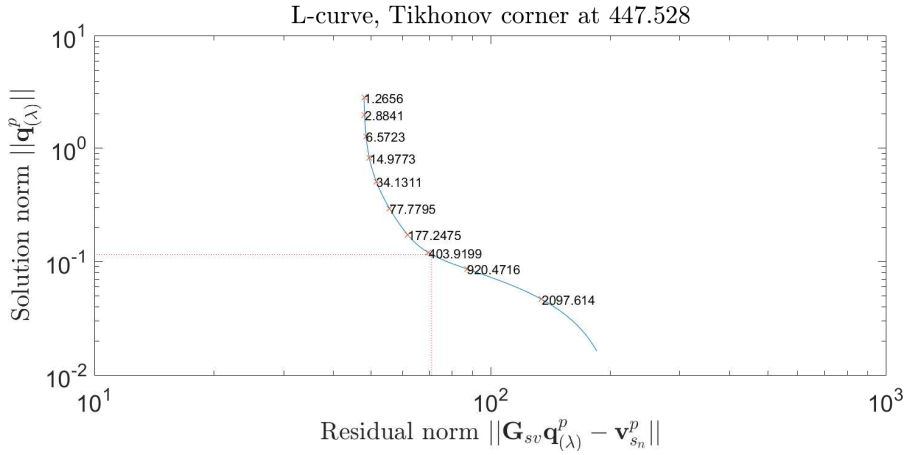

Figure 5.3: L-curve to choose the Tikhonov regularization parameter λ

```
% Principal components whose relevance is greater then the 0.1%
Lopt = find(explained > 0.1, 1, 'last' );
```

5.2.3 Computing the driving vector of the dictionary

To solve the NAH problem, as discussed in Sec. 4.5 we have to compute the driving vector $\boldsymbol{\gamma}$ as illustrated in Eq. (4.26). To compute the solution we use the LASSO regularization. This operation can be done using this MATLAB® code

```
% LASSO regression
[gammaLASSO,~,~,~] = spg_lasso(D,ph,norm(ph,1));
```

The `spg_lasso` function is included in the *spgl1* toolbox - Copyright © 2008, Ewout van den Berg and Michael P. Friedlander [21], [22]. With reference to Eq. (4.27) the variable `D` represents the matrix product $\mathbf{G}_{hp}\mathbf{D}$ and `ph` corresponds to the vector $\mathbf{p}_h$ of the pressure measured on the hologram plane. The third parameter of the function corresponds to the parameter $\mathcal{T}$ used to fix the amount of the regularization. It is chosen equal to the ℓ_1-norm of the vector $\mathbf{p}_h$. The ℓ_1-norm is computed by `norm(ph,1)`.

Chapter 6

Experiments

In this chapter we validate the proposed methodology. In particular, the experimental results obtained from acoustic measurements acquired over a rectangular aluminium plate. We describe the source geometry and the physical parameters used. We illustrate the measurement setup and then we will show our results compared with those obtained with the classical ESM implementation and those achieved by the method described in Sec. 3.2 by means of the NACHOS toolbox [2]. Successively, we will assess the robustness of the proposed method against additive measurement noise. Finally, we will show simulation results relative to the analysis of a complex surface, compared to those provided by the classical implementation of the ESM. To this end, we considered a violin top plate, which presents a non-convex curved surface.

6.1 Validation

In this section we focus our attention to the results achieved by analysing a rectangular aluminium plate. We illustrate the source geometry and the physical parameters used, the measurement setup and finally we present the results. The pressure measurements used are those included in the NACHOS database provided by the authors of [2].

6.1.1 Plate geometry and physical parameters dataset

The experimental setup is that described in [2]. In particular, the aluminium rectangular plate has dimensions 500 mm×400 mm×4 mm (L×W×H). The four corners of the panel are put on light rubber silent blocks to approach free boundary conditions.

As explained in Sec. 4.2, we computed the theoretical normal velocity of the plate by means of FEA analysis, considering different combinations of the physical parameters. More specifically, we have varied the Young's modulus, the Poisson's ratio, the shear moduls and the density according to the values associated to different alluminium alloys. The list of alloys and parameters considered are reported in Tab. A.1 of Appendix A.

6.1.2 Experimental setup

As described in [2], the aluminium plate was excited by an impulse hammer, positioned under the plate itself. The excitation point is located in such a way to excite a significant number of modes.

Microphones setup

The NACHOS database includes 1920 measurement points. The microphones are positioned on a rectangular regular grid of 48×40 points with dimensions 550 mm × 450 mm, therefore the spacing between microphones is approximately equal to 11 mm in each direction. The distance between the hologram plane and the plate is equal to 20 mm.

In our experiments we do not use all the information provided by the 1920 measurements points, but only a very small subset. In our test we consider two configurations: a regular microphone array and a random microphone array. The second array is made by randomly selecting a subset of 1920 measurement points. For each configuration we use 16, 32 and 64 microphones since we want to test our method with different setups, but using a limited number of microphones. In Sec. 6.1.3 we will illustrate experimental results using three configurations with 16, 32 and 64 microphones respectively.

D-ESM setup

The equivalent sources are positioned on a plane below the plate. The distance between the bottom face of the plate and the equivalent sources plane is equal to 20 mm. The equivalent sources are positioned on a regular grid of 48×40 points with dimensions 480 mm × 400 mm. The grid spacing is equal to 10 mm in each direction. Fig. 6.1 depicts the positions of the plate, the microphones and the equivalent sources. For reasons of clarity we have shown only a few microphones. As shown in Fig. 6.1(b) the origin of the axes is in the middle of the top face of the plate. Therefore, with reference to Fig. 6.1(a), $z_s = 0\,\text{mm}$, $z_h = 20\,\text{mm}$ and $z_q = -24\,\text{mm}$.

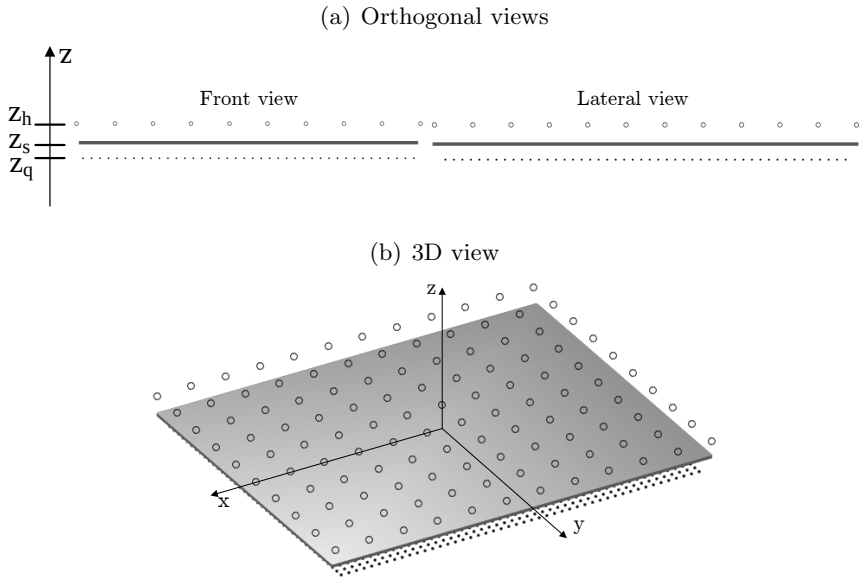

Figure 6.1: Positioning of the equivalent sources plane and the hologram plane respect to the rectangular plate. ○ identifies microphones positions and • identifies equivalent sources positions.

Ground truth measurements

The NACHOS database [2] includes also the groundtruth data, obtained by measuring the plate velocity using a laser vibrometer. The measurements were performed on a grid of 50 ×40 points. The lattice spacing was equal to 10 mm in each direction. We will use this ground truth data as a reference for validating the proposed NAH technique.

Evaluation metric

The analysis is performed in the frequency range between 28 and 3.6 kHz. The correlation coefficient is defined as

$$C(\mathbf{v}, \hat{\mathbf{v}}) = \frac{1}{N-1} \sum_{n=1}^{N} \left(\frac{\mathbf{v}_n - \mu_{\mathbf{v}}}{\sigma_{\mathbf{v}}} \right) \left(\frac{\hat{\mathbf{v}}_n - \mu_{\hat{\mathbf{v}}}}{\sigma_{\hat{\mathbf{v}}}} \right) \times 100 \tag{6.1}$$

where $\mathbf{v}$ corresponds to the ground truth velocity and $\hat{\mathbf{v}}$ corresponds to the reconstructed velocity, μ is the mean value and σ is the variance of $\mathbf{v}$ and $\hat{\mathbf{v}}$ respectively, N is the number of elements of the mesh.

6.1.3 Experimental results

In this section we analyse the experiments conducted on the rectangular aluminium plate using real measurements. In particular, we present the results related to the reconstructed modes of vibration and we compare them with the ground truth data. We include also a comparison with the classical ESM method and the NACHOS method.

Results

In Fig. 6.2 we show some results obtained by the proposed method (D-ESM from now on) in comparison with those provided by the ESM and the NACHOS techniques. This results are retrieved using 64 microphones distributed on a regular grid. We consider three modes of vibration at 78, 267 and 402 respectively. As we can see in figure, the modes retrieved by D-ESM present a very good correspondence of the *nodal line* with reference to the ground truth. This is also confirmed by the high correlation scores ($C_{78\text{ Hz}} = 94.9\%$, $C_{267\text{ Hz}} = 93.6\%$ and $C_{402\text{ Hz}} = 93.5\%$).

In a vibrating plate, the nodal lines are those lines which remain at rest while the other parts of the body are in a state of vibration.

Looking at the ESM and NACHOS results we can see that they poorly reconstruct the mode shapes, in particular the correspondence of the nodal lines with respect to the ground truth is not perfect. Moreover we can observe that they tend to centralize the *anti-nodes*, visible in yellow. Anti-nodes are points at which the amplitude of one of the two kinds of displacement in a standing wave has maximum value. Generally the other kind of displacement has its minimum value at this points. For these reasons, correlation scores for ESM and NACHOS are quite low.

Fig. 6.3 shows some results obtain using our method considering different configurations. In particular we present the results obtained with 16, 32 and 64 microphones respectively, using a regular array configuration. We show three modes at 78, 215 1636 Hz respectively. As we can see the results related to 32 and 64 microphones are good. The 16 microphones configuration results, instead, present a not perfectly match for the third mode.

We now analyse in depth the results, considering the correlation score at all the frequencies in the range from 28Hz to 3.6kHz. The diagram in Fig. 6.4 depicts the correlation between the ground truth and the results obtained by D-ESM, ESM and NACHOS techniques using 16 microphones on a regular grid. As we can see, looking at the D-ESM curve in Fig. 6.4, 16 microphones, disposed on a regular grid, are not sufficient to guarantee good mode shape estimation. Using only 16 microphones the dictionary

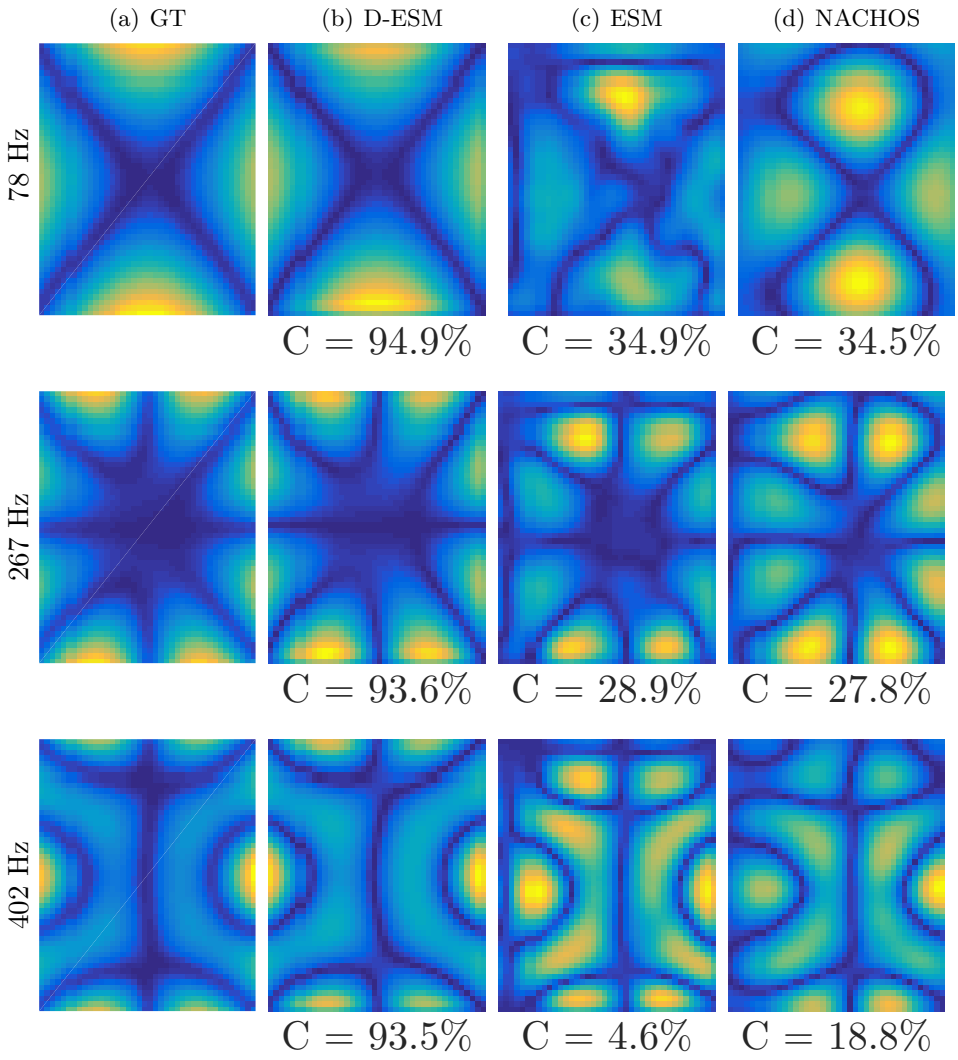

Figure 6.2: Rectangular plate results using regular microphones array. In figure is shown the absolute value to highlight the nodal lines (top view).

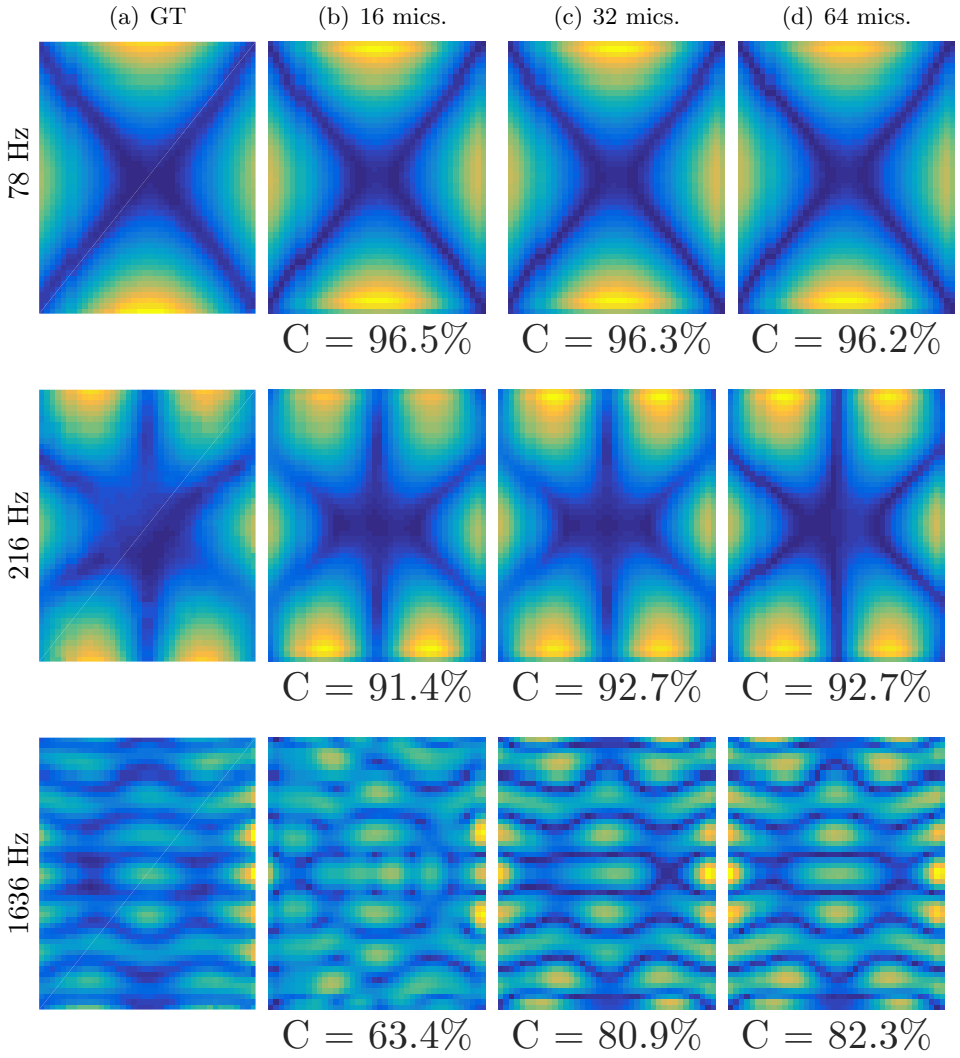

Figure 6.3: Rectangular plate D-ESM results using 16, 32 and 64 regular microphones array. In figure is shown the absolute value to highlight the nodal lines (top view).

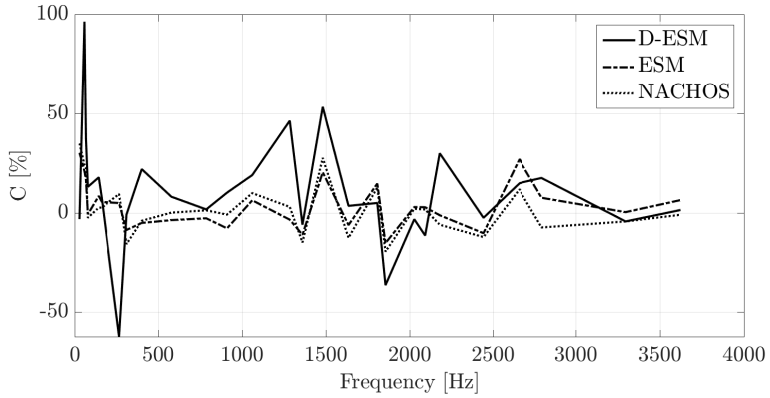

Figure 6.4: Correlation between the ground truth and the D-ESM, ESM and NACHOS techniques results using 16 regular microphones arrays.

subset search cannot retrieve correctly the mode index. The failure is due to the fact that the search algorithm relies on a severe under-sampling of the acoustic pressure field , used to compute the cost function described in Sec. 4.5.1. Moreover there is a high probability that the microphones match the positions of the nodal lines and therefore they cannot provide useful information. To overcome this limitation we considered the possibility of using a random distribution of microphones. Doing so, we improved the accuracy of D-ESM, as shown by the correlation curve reported in Fig. 6.5. Comparing the results in Fig. 6.4 and Fig. 6.5, we can clearly observe that, when the number of microphones is limited, with a random microphone array we can achieve better results. Moreover Fig. 6.5 shows the results obtained with ESM and NACHOS techniques using the same configuration. Looking at the D-ESM curve in Fig. 6.5, we can see that our method achieved good results until approximatively 1.2 kHz outperforming the ESM and NACHOS results.

We now increase the number of microphones used for modal analysis. Fig. 6.6 depicts the results using 32 microphones regular array. As in the previous case the analysis is performed in the frequency range between 28 and 3.6 kHz. As we can see, comparing the D-ESM curve, with that in Fig. 6.4, the results obtained are better.In fact, using a greater number of microphones allows us to obtain more stable results related to the dictionary subset search. As we can see the performances of our method significantly improve and we can obtain good results approximatively until 1.7 kHz.

Finally we present the results using a 64 microphones regular array. With reference to Fig. 6.7 we can observe that in this case we achieve good results until 2.5 kHz.

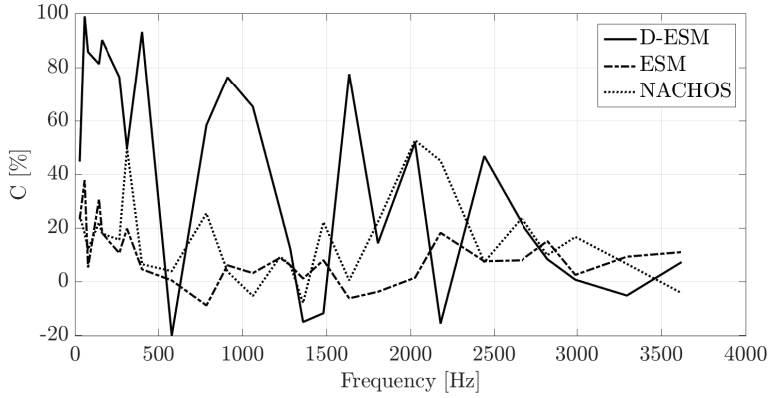

Figure 6.5: Correlation between the ground truth and the D-ESM, ESM and NACHOS techniques results using 16 random microphones array.

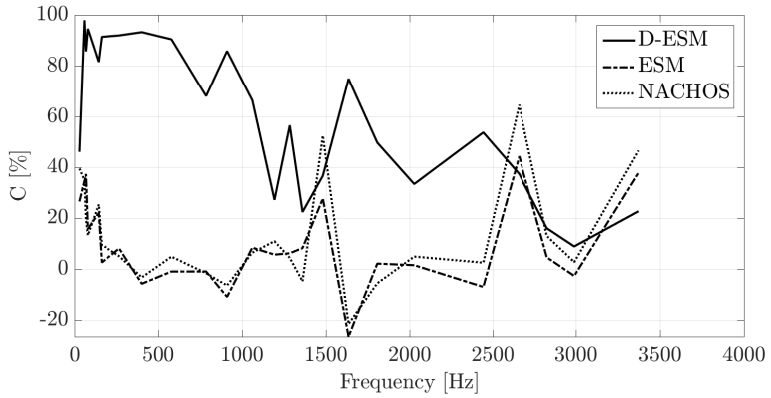

Figure 6.6: Correlation between the ground truth and the D-ESM, ESM and NACHOS techniques results using 32 regular microphones array.

We also tested the D-ESM method using random distributions of 32 and 64 microphones. In this case we did not observe valuable improvements with respect to the case of using regular microphone grids. For the sake of completeness, we report the average correlation scores in Tabs. 6.1 and 6.2, which show that correlation remains unvaried using regular or random array of 32 and 64 microphones.

6.1.4 Robustness against measurement noise

An important aspect of the NAH techniques is the noise rejection. Usually an essential requirement is that the acoustic of the room has to be controlled. The measurements have to be acquired with many microphones and in a special room called anechoic chamber. This room assures a perfectly acoustic

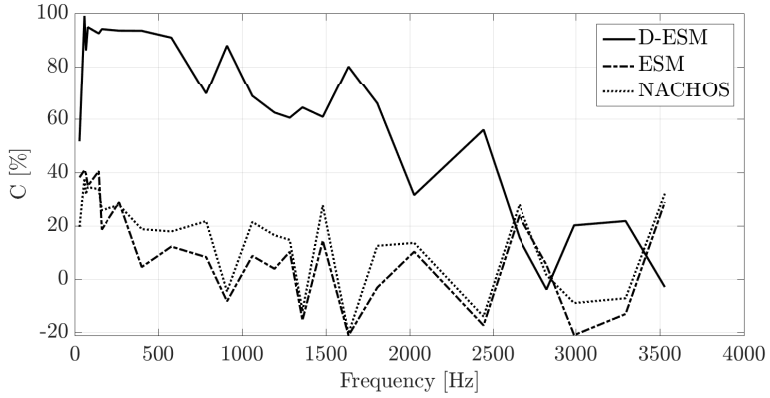

Figure 6.7: Correlation between the ground truth and the D-ESM, ESM and NACHOS techniques results using 64 regular microphones array.

Nb. of mics.	D-ESM	ESM	NACHOS
16	9.0%	3.1%	2.3%
32	56.9%	8.6%	12.5%
64	61.0%	11.1%	14.4%

Table 6.1: Mean correlation values for 16, 32 and 64 regular microphones arrays for the D-ESM, ESM and NACHOS methods.

isolation and moreover an almost null reverberation. On the other hand the building/rent cost of this room is very high as is the cost of a very large microphone system.

Our method aims at being robust in those situations where it is not possible to use a great number of microphones. Moreover our method intrinsically presents a robust behaviour in the presence of measurements noise. An example could be the reverberation. The measurements have been carried-out in a non-ideal room [2], therefore reverberation and background noise are present. The results presented in Sec. 6.1.3 show that our method achieves good results using a limited number of microphones if compared with the state of the art. In this section we stress further our method. For sim-

Nb. of mics.	D-ESM	ESM	NACHOS
16	37.5%	9.2%	14.4%
32	54.6%	25.5%	33.6%
64	60.5%	21.3%	45.0%

Table 6.2: Mean correlation values for 16, 32 and 64 random microphones arrays for the D-ESM, ESM and NACHOS methods.

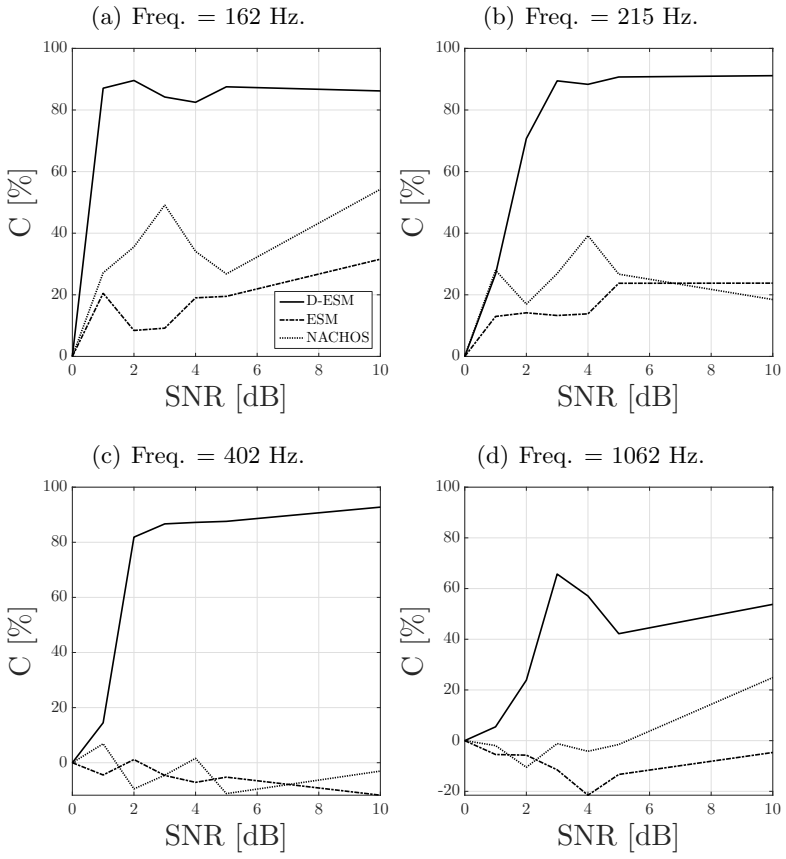

Figure 6.8: Perfomances of the D-ESM, ESM and NACHOS techniques at low SNR. The legend uses is the same for all the diagrams.

plicity, we add uncorrelated white noise to the real measurements used in Sec. 6.1.3 with different Signal to Noise Ratio (SNR). We have to clarify that the level of the SNR is computed considering the measurements of the NACHOS database noise free. Therefore the real SNR could be even lower.

Fig. 6.8 shows the diagrams of the performances of the three techniques (D-ESM, ESM and NACHOS) using 16 microphones random array. We consider four frequencies: 162, 215, 402 and 1062 Hz. We add white noise with different SNR: 1, 2, 3, 4, 5 and 10 dB. As we can see our method with only 2/3 dB of SNR can achieved good and stable results outperforming the other techniques. This is true for the first three frequencies analysed, the fourth instead present a non perfect behaviour. This is due to the fact that we are approaching the frequency limit of the 16 microphones configuration. For 32 and 64 microphone arrays we obtained similar results.

6.2 A perspective on complex surfaces: simulations on a violin top plate

In the perspective of analysing more complex surfaces, we consider, as example, the modal analysis of acoustic musical instruments. A very interesting musical instrument under the vibratory aspect is the violin. Violins present a complex structure: top and back plates have a complex shape, are not planar and exhibit a non-symmetric vibration behaviour due to the presence of the bass bar and of the sound post. Moreover top plates present two apertures with complex shape, the so called f. These aspects make the vibratory and consequently the acoustic behaviour quite unpredictable. In our case we consider only the top plate of the violin. From a practical point of view studying how a musical instrument works provides a series of technical tools and an improved knowledge, that can be used by violin makers to enhance their work. For example, when a luthier is making a violin top plate and wants to verify whether the tuning of the top plate is correct, he/she can do it not only by relying on his/her personal experience, but also by means of objective measurements.

The NAH is a contactless technique therefore we can analyse musical instruments in a minimally invasive manner without damaging them or their thin layer of varnish. The analysis, however, cannot be non-invasive at all since it is necessary, in any case, to excite mechanically the instrument. The mechanical excitation can be performed tapping the instrument, by means of a special hammer, in a "safe" point (e.g the violin bridge).

6.2.1 Violin top plate geometry and physical parameters dataset

Fig. 6.9 depicts the exterior and interior views of a violin top plate where bass bar are cleary visible [23]. The violin top plate is made of spruce fir. The dataset of physical parameters of the wood is reported in Tab. A.2 in Appendix A. To create the dataset we considered different types of spruce fir at different seasoning lumber stages. As we can see the bass bar makes the violin top non-symmetric.

6.2.2 Simulation setup

The setup used to perform the simulations is shown in Fig. 6.10. For reasons of clarity, we have shown only a few microphones. As in the rectangular plate case, microphones and equivalent sources are positioned on a grid above and below the violin top plate.

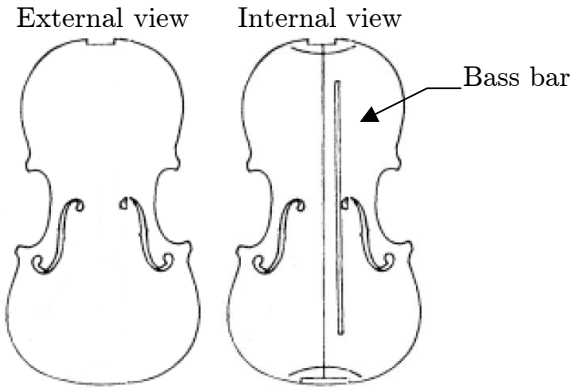

Figure 6.9: Interior view of the violin top plate [23].

Microphones setup

We use two different configurations in this case: 32 and 64 microphones regular arrays. Due to complexity of the problem, from preliminary simulations we observed that in this case it is not possible to use 16 microphones.

With reference to the 32 microphones array, the microphones are positioned on a regular grid of 8×4 points with dimension 400 mm × 240 mm. The grid spacing is therefore equal to 50 mm in x direction and 60 mm in y direction. Since the top plate is curved, the distance between the violin top plate and the hologram plane is not constant. The minimum distance, between the measurement points and the violin plate is 20 mm. In our simulations we do not use all the measurements provided by the microphones array, but only a small subset.

On the other configuration the 64 microphones are positioned on a regular grid of of 8×8 points with dimension 400 mm × 240 mm. The grid spacing is therefore equal to 50 mm in x direction and 30 mm in y direction. As in the previous case, since the top plate is curved, the distance between the violin top plate and the hologram plane is not constant. The minimum distance, between the measurement points and the violin plate is 20 mm.

D-ESM setup

The equivalent sources are positioned on a plane below the violin top plate. The distance between the lowest point of the violin top plate and the equivalent sources plane is equal to 20 mm. The equivalent sources are positioned on a lattice with 20×12 points with dimensions 350 mm × 210 mm. The lattice spacing is equal to 17.5 mm in each direction.

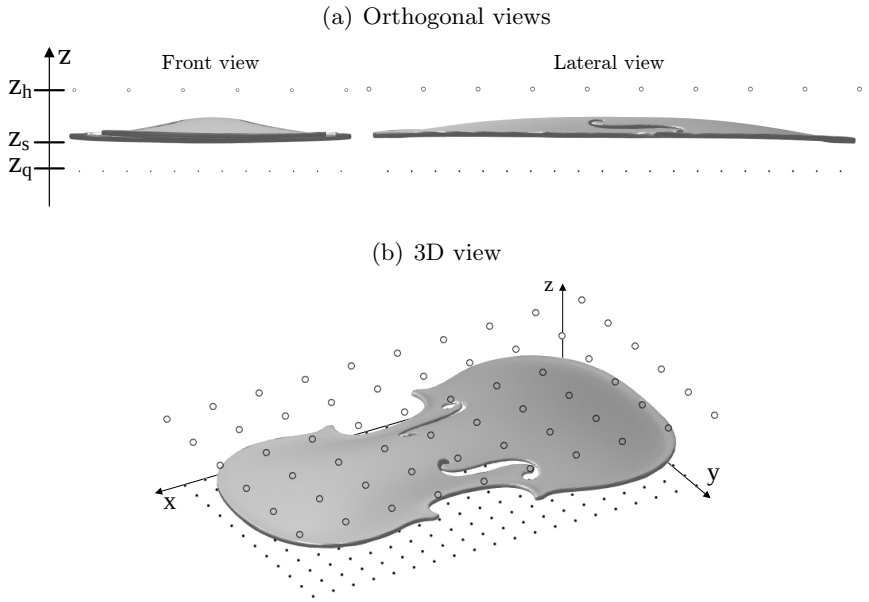

Figure 6.10: Positioning of the equivalent sources plane and the hologram plane respect to the violin top plate. ○ identifies microphones positions and • identifies equivalent sources positions.

Ground truth computation

The ground truth is obtained by means of the FEA starting from the physical parameters and the CAD model of the violin top plate. The acoustic pressure field is computed using the Boundary Element Method (BEM) [24] starting from the normal velocity of the source surface computed by means of FEA. To simulate the acoustic pressure field we used the BEM acoustics toolbox [25]

6.2.3 Simulation results

In this section we analyse the simulation results related to the violin top plate. We present qualitative results which show the mode shape of the first, fourth and fifth mode of the violin top plate. Then we present quantitative results showing the performances of our method using 32 and 64 microphones array. Finally we make some considerations about noise measurements.

Results of reconstructed modes of vibration

In this section we present some results about violin top plate simulations Fig. 6.11 depicts three reconstructed mode shapes, respectively at 90, 258

and 336 Hz, corresponding to the first, fourth and fifth mode of the violin top plate. We considered a 64 microphones regular array. Fig. 6.11 depicts the FEA ground truth, the results obtained with the D-ESM method using the optimal subset search and the classical ESM results. Note that, since the surface is curved, the NACHOS method can't be used in this case. As we can see, the D-ESM method achieves very good results. The correlation coefficient is equal to 91.2% for the first mode, to 83.4% for the fourth mode and 84.1% for the fifth mode. Instead, the ESM method reconstructs the nodal lines almost correctly, but, as we can see, the position of the anti-nodes are mostly wrong. In particular for the fourth mode we can observe the anti-nodes, in yellow, in a centered position, instead decentered as depicted by the ground truth. The same behaviour can be observed for the fifth mode. Moreover we can see that the nodal lines reconstructed are not perfectly corresponding to the ground truth. In fact the ESM correlation coefficients are equals to 74.5% and 28.8% and 33.5% for the first, fourth and fifth mode respectively.

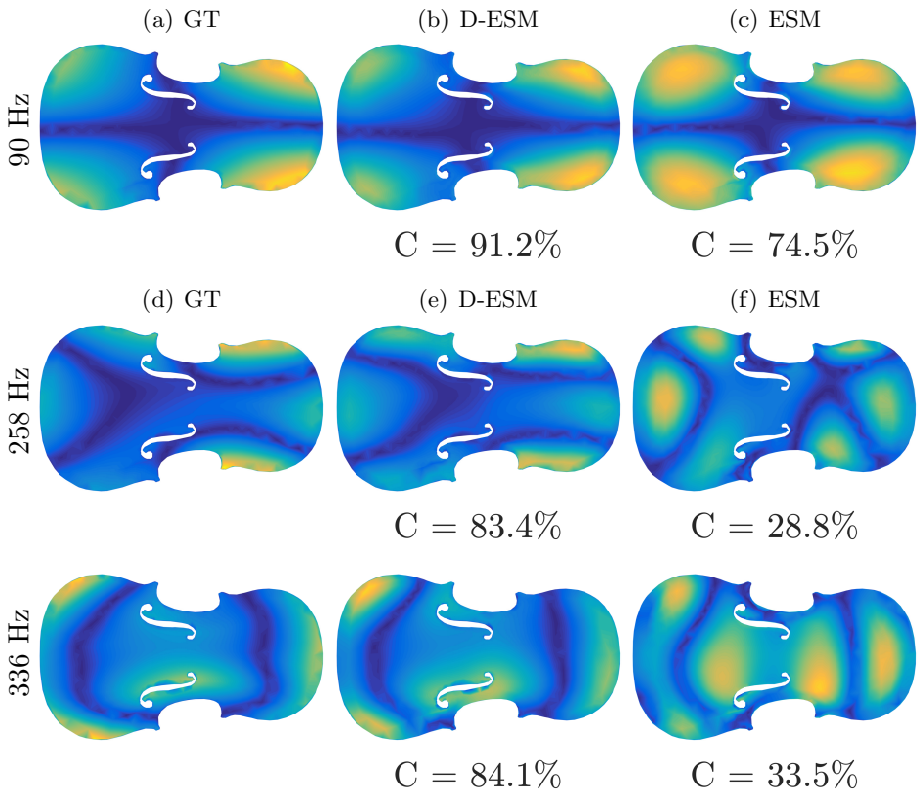

Figure 6.11: Violin top plate results using 64 random microphones array. In figure is shown the absolute value to highlight the nodal lines (top view).

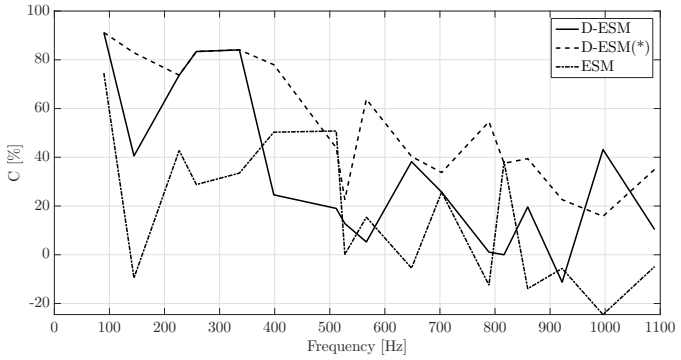

Figure 6.12: Correlation between the ground truth and the D-ESM, D-ESM with FEA-based search and ESM techniques results using 32 regular microphones array.

The diagram in Fig. 6.12 depicts the correlation between the ground truth and the results obtained by the D-ESM and the ESM techniques using 32 microphones. The analysis is performed in the frequency range between 90 and 1.1 kHz. The D-ESM curve, as in the rectangular plate case, at some frequencies drops down abruptly. We noticed that this happens when the dictionary subset search fails. The D-ESM(*) curve shows the results which we would achieve if the dictionary subset search provides perfect results. More specifically, to compute the D-ESM(*) curve we skip the dictionary subset search, and we selected the optimal dictionary subset relying to the FEA ground truth. In this way we obtain more accurate results for the selection of the optimal dictionary subset and therefore higher accuracy in mode-shape estimation. This confirms that the optimal subset search, as explained in Sec. 4.5.1, is a critical task. Fig. 6.13 depicts the same results using 64 microphones array. As we can see from the diagrams the D-ESM can achieve almost good results, especially at low frequencies. As in the previous case we depict the D-ESM(*) curve which shows the results that could be obtained if the dictionary subset search provides better information for the selection of the dictionary subset.

Give the results, we can state that using 32 microphones we obtain good reconstruction of the mode shapes and using 64 microphones we can achieve very good results.

6.2.4 Robustness against measurement noise

As in the aluminium rectangular plate, we tested our method also in the presence of hight level of noise. For simplicity, as in the rectangular plate case, we add uncorrelated white noise to the real measurements used in

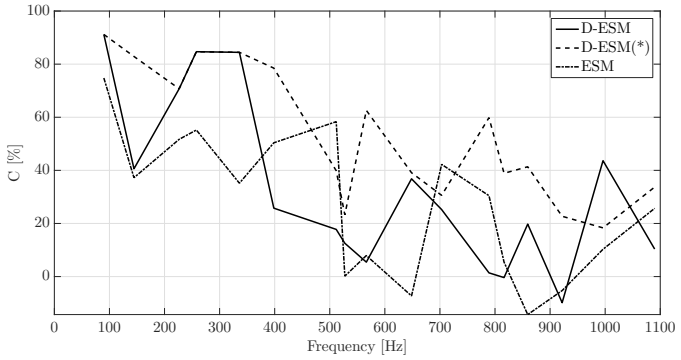

Figure 6.13: Correlation between the ground truth and the D-ESM, D-ESM with FEA-based search and ESM techniques results using 64 regular microphones array.

Sec. 6.2.3 with different Signal to Noise Ratio (SNR). We observed that our method presents the same behaviour as in the case of simplest geometry. We made the simulations for all the correctly retrieved modes of the violin top plate. Fig. 6.14 depicts the results obtained, related to the fifth mode of vibration. The diagram show the results of the D-ESM compared with those obtain with the ESM technique.

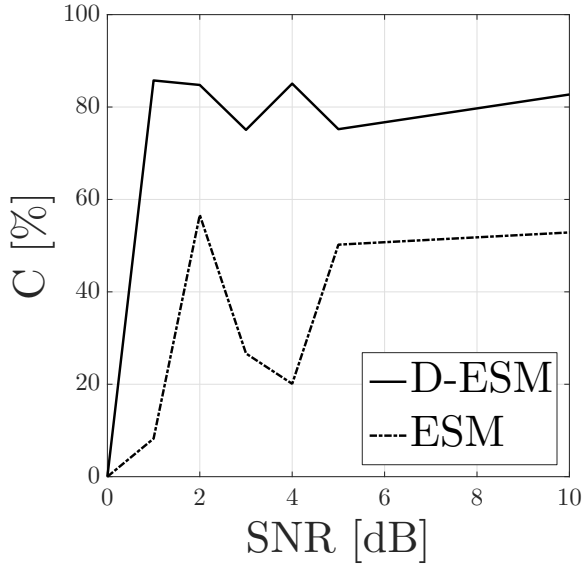

Figure 6.14: Performances of the D-ESM and ESM techniques at low SNR.

Chapter 7

Conclusions and Future Works

In this thesis we have proposed a novel methodology for Near-field acoustic holography to deal with arbitrary shape geometries using a limited number of microphones. The proposed technique extends the equivalent source method (ESM) proposed in the literature as an efficient approximation to BEM and IBEM methods. Unfortunately, the standard ESM technique presents some criticisms related to the positioning of the equivalent sources, and exhibits low robustness against measurement noise.

The method proposed in this thesis exploits some a-priori knowledge, related to the fact that the modes shape and also the equivalent source weights are slightly changed varying the physical parameter of the material. We thus proposed a dictionary-based approach to search for the ESM solution. More specifically, the solution is found selecting from the dictionary the best entries, according to the pressure measured on the hologram plane, and than propagating them to the object surface.

Since we are particularly interested in using a limited number of microphones to have a simpler acquisition system, to reduce the hardware cost and the wiring complexity, we tested our method under these conditions.

We have noticed that using a limited number of microphones imposes some constrains. The main problem is due to the spatial aliasing which limits the analysis frequency range. We have seen that using a dictionary approach it is possible to overcome this limitation. A proof of this is the fact that using only 16 microphones on a measurement aperture of 550 mm $\times$450 mm wide, we can achieve moderately good results approximatively until 1.2 kHz, while state-of-the-art techniques require an higher number of microphones to achieve the same results. Increasing the number of microphones

guarantees better and more stable results. Using 32 microphones we can raise the frequency limit until 1.7 kHz obtaining good results with respect to the ESM and NACHOS. Using a 64 microphones array we can extend the frequency limit of our method to 2.5 kHz and with this configuration we obtain results comparable to those provided by NACHOS. As shown by experimental results using a random distribution of microphones allows us to obtain better results when the number of microphones is very low.

Another critical point is the presence of measurement noise. If we cannot acquire the measurements in an anechoic chamber the measurements themselves will have a certain amount of background noise and reverberation. Moreover we have to consider the instrumental and electronic noise of the acquisition system. Our techniques, using a dictionary based approach and seeking the solution in a sparse domain guarantees good results in the presence of high level of noise. Experiments show that it is possible to obtain good results even for very low SNR values.

Finally, simulations provide good results also analysing a complex surface, as that of a violin top plate.

The performance of the proposed D-ESM technique is strictly dependent on the accuracy of search of the optimal dictionary subset. The search result is influenced by many factors especially by the number of measurements available and the level of noise. In particular, experimental results suggest that using a limited number of microphones negatively influences the identification of the correct subset of the dictionary. As shown by the experimental results, using 32 or 64 microphones arrays guarantees better search results. An open issue is the development of a stable algorithm for the optimal subset search which works in critical condition.

Another aspect that should be more more deeply investigated is that relative to the use of random microphones array especially when the number of microphones is very limited.

Finally, there is the need to make real measurements using complex geometries.

Appendix A

Physical parameters set

A.1 Aluminium

Tab. A.1 depicts the physical parameters of the pure aluminium a some aluminium alloys. In particular, it shows the density ρ, of the material, expressed in kg/m^3, the Young's modulus E, expressed in GPa = 10^9 Pa, the Poisson's ration ν, and in the last column reports the shear modulus G, in GPa.

Table A.1: Physical parameters of aluminium and aluminium alloys [26].

Material	ρ_0 [kg/m^3]	E [GPa]	ν	G [GPa]
Pure Al	2700	69.0	0.34	25.0
1050 H14	2705	69.0	0.33	26.0
1030H12	2705	68.9	0.33	26.0
2024-T3	2780	73.1	0.30	28.0
2090-T3	2590	76.0	0.34	28.0
6061-O	2700	68.9	0.33	26.0
7075-T6	2810	71.7	0.33	26.9
7075-T66	2800	72.0	0.33	27.0

A.2 Wood: spruce fir

Tab. A.2 reports the physical parameters of the spruce fir. This table is incomplete since the parameters of the wood are not perfectly defined, as in the case of the aluminium, and therefore it is hard to retrieve a complete set of parameters. This is due to de fact that the wood parameter vary in according to the climatic region of grow, to the temperature, to the level of moisture presents in the wood fibres and also to the seasoning lumber stage. In particular Tab. A.2 depicts the density of the wood ρ, in kg/m^3. The Young's modulus E, the Poisson's ratio ν, and the shear modulus G, are reported for each direction, since the wood is an orthotropic material. The Young's and shear modulus are depicted in MPa = 10^6 Pa.

Table A.2: Physical parameters of spruce fir [27].

ρ_0 [kg/m^3]	380	400	420	430	440	450	470	500
E_x $[MPa]$	9907	10200	14900	-	-	-	-	-
E_y $[MPa]$	690	790	1225	-	-	-	-	-
E_z $[MPa]$	390	714	-	-	-	-	-	-
ν_{xy}	0.44	-	-	-	-	-	-	-
ν_{xz}	0.38	-	-	-	-	-	-	-
ν_{yz}	0.47	-	-	-	-	-	-	-
G_{xy} $[MPa]$	750	-	-	-	-	-	-	-
G_{xz} $[MPa]$	770	-	-	-	-	-	-	-
G_{yz} $[MPa]$	36	-	-	-	-	-	-	-

Bibliography

[1] Earl G Williams. *Fourier acoustics: sound radiation and nearfield acoustical holography*. Academic press, 1999.

[2] Gilles Chardon, Laurent Daudet, Antoine Peillot, François Ollivier, Nancy Bertin, and Rémi Gribonval. Nearfield acoustic holography using sparsity and compressive sampling principles.

[3] JG Ih. Acoustic holography based on the inverse-bem for the source identification of machinery noise. 2007.

[4] Yong-Bin Zhang, Finn Jacobsen, Chuan-Xing Bi, and Xin-Zhao Chen. Near field acoustic holography based on the equivalent source method and pressure-velocity transducers. *The Journal of the Acoustical Society of America*, 126(3):1257–1263, 2009.

[5] William Cronk Elmore, William C Elmore, and Mark A Heald. *Physics of waves*. Courier Corporation, 1969.

[6] Arthur W Leissa. Vibration of plates. Technical report, DTIC Document, 1969.

[7] Julian D Maynard, Earl G Williams, and Y Lee. Nearfield acoustic holography: I. theory of generalized holography and the development of nah. *The Journal of the Acoustical Society of America*, 78(4):1395–1413, 1985.

[8] Earl G Williams and JD Maynard. Holographic imaging without the wavelength resolution limit. *Physical Review Letters*, 45(7):554, 1980.

[9] Scott Shaobing Chen, David L Donoho, and Michael A Saunders. Atomic decomposition by basis pursuit. *SIAM review*, 43(1):129–159, 2001.

[10] Earl G Williams. Regularization methods for near-field acoustical holography. *The Journal of the Acoustical Society of America*, 110(4):1976–1988, 2001.

[11] Augustus Edward Hough Love. The small free vibrations and deformation of a thin elastic shell. *Philosophical Transactions of the Royal Society of London. A*, 179:491–546, 1888.

[12] Per Christian Hansen. Analysis of discrete ill-posed problems by means of the l-curve. *SIAM review*, 34(4):561–580, 1992.

[13] Per Christian Hansen. The truncatedsvd as a method for regularization. *BIT Numerical Mathematics*, 27(4):534–553, 1987.

[14] Mingsian R Bai, Ching-Cheng Chen, and Jia-Hong Lin. On optimal retreat distance for the equivalent source method-based nearfield acoustical holography. *The Journal of the Acoustical Society of America*, 129(3):1407–1416, 2011.

[15] Nicolas P Valdivia and Earl G Williams. Study of the comparison of the methods of equivalent sources and boundary element methods for near-field acoustic holography. *The Journal of the Acoustical Society of America*, 120(6):3694–3705, 2006.

[16] Olgierd Cecil Zienkiewicz, Robert Leroy Taylor, Olgierd Cecil Zienkiewicz, and Robert Lee Taylor. *The finite element method*, volume 3. McGraw-hill London, 1977.

[17] Hervé Abdi and Lynne J Williams. Principal component analysis. *Wiley Interdisciplinary Reviews: Computational Statistics*, 2(4):433–459, 2010.

[18] Robert Tibshirani. Regression shrinkage and selection via the lasso. *Journal of the Royal Statistical Society. Series B (Methodological)*, pages 267–288, 1996.

[19] Gene H Golub, Michael Heath, and Grace Wahba. Generalized cross-validation as a method for choosing a good ridge parameter. *Technometrics*, 21(2):215–223, 1979.

[20] Andrej Nikolaevich Tikhonov and Vasiliy Yakovlevich Arsenin. Solutions of ill-posed problems. 1977.

[21] E. van den Berg and M. P. Friedlander. Probing the pareto frontier for basis pursuit solutions. *SIAM Journal on Scientific Computing*, 31(2):890–912, 2008.

[22] E. van den Berg and M. P. Friedlander. SPGL1: A solver for large-scale sparse reconstruction, June 2007. http://www.cs.ubc.ca/labs/scl/spgl1.

[23] Walter Kolneder and Reinhard G Pauly. *The Amadeus book of the violin: construction, history, and music.* Amadeus Pr, 1998.

[24] Prasanta Kumar Banerjee and Roy Butterfield. *Boundary element methods in engineering science*, volume 17. McGraw-Hill London, 1981.

[25] Michael Stütz. Bem acoustics. *BEM acoustics,[Online]. Available: http://www.bemacoustics.com*, 2009.

[26] LLC MatWeb. Material property data. *MatWeb,[Online]. Available: http://www. matweb. com*, 2014.

[27] L. Dotta G. Zugliani. Legno di risonanza. *Sherwood - Foreste ed alberi oggi*, 154-155(5-6):8–19, 2009.